Major and trace elements exchanges during fluid-rock interaction at ultraslow-spreading oceanic lithosphere: Example of the South West Indian Ridge (SWIR)

Lucile Dessimoulie, Adélie Delacour, Damien Guillaume, June Chevet, Jean-Yves Cottin

MAJOR AND TRACE ELEMENTS EXCHANGES DURING FLUID-ROCK INTERACTION AT ULTRA-SLOW SPREADING OCEANIC LITHOSPHERE: EXAMPLE OF THE SOUTH WEST INDIAN RIDGE (SWIR)

Lucile DESSIMOULIE[a], Adélie DELACOUR[a]*, Damien GUILLAUME[a], June CHEVET[a], and Jean-Yves COTTIN[a]

[a] *Université de Lyon, UJM-Saint-Etienne, LMV, UMR 6524, F-42023 SAINT-ETIENNE, France*

Corresponding author: adelie.delacour@univ-st-etienne.fr

1. Introduction

Since the end of the 70's, numerous studies demonstrated that fluid-rock interactions occurring within the oceanic lithosphere play a major role in the biogeochemical cycles. Earlier studies focused on fluid-rock interaction in basaltic crust and reported chemical element fluxes at the Earth surface, through high and low-temperature hydrothermal fluids venting, as well as significant changes in mineralogical and chemical compositions of the MOR-type basaltic rocks (e.g., Alt, 2004 for a review). More recent studies investigated the interaction of seawater-derived hydrothermal fluids with exhumed mantle rocks (i.e., abyssal peridotites). This process, known as serpentinization, is now recognized as playing a key role in the chemical elements exchanges between deep (mantle) and superficial (ocean, crust, biosphere) Earth reservoirs (Alt et al., 2013; Deschamps et al., 2011; Hattori and Guillot, 2003).

Peridotites are strongly modified during serpentinization in terms of physical properties (O'Hanley, 1996; Toft et al., 1990), oxidation degree (Andreani et al., 2013; Evans, 2008), mineralogical assemblages (Mével, 2003; O'Hanley, 1996) and chemical composition. Indeed, previous works on the Mid-Atlantic Ridge (MAR) and the South West Indian Ridge (SWIR) showed that serpentinites can be enriched, but also depleted, in several chemical elements, such as sulfur (Alt et al., 2013 and references within), carbon (Delacour et al., 2008a), Light Rare Earth Elements (LREE, such as europium Eu), and Fluid Mobile Elements (FME: U, Pb, B, As, Sb, Cs, Sr, Ba, Li, B; (Deschamps et al., 2011, 2012, 2013 and references within; Frisby et al., 2016; Lee et al., 2008; Niu, 2004; Vils et al., 2008) depending on serpentinization conditions and geological setting. Characterizing serpentinization processes and the chemical compositions of serpentinites are thus of crucial importance to better understand the fluxes in chemical elements between the ocean and the oceanic lithosphere. Understanding and quantifying the mass transfer during serpentinization would also be valuable in a more global

scale to i) better define the speciation and concentrations of elements that are either released to the fluids, sustaining then deep and shallow biosphere, or stored into oceanic serpentinites, and ii) determine the composition of the oceanic lithosphere entering subduction and therefore of the fluids that will be released to the mantle wedge (Hattori and Guillot, 2003).

Studying element transfers related to serpentinization of abyssal peridotites is however challenging because of the non-uniqueness of peridotite protolith, the common lack of primary mineral relics due to the advanced stages of serpentinization of oceanic peridotites, the multiple stages of serpentinization affecting the peridotites, and the low-temperature post-serpentinization processes. Indeed, low-temperature alteration processes can occur secondary to serpentinization, transforming the serpentine minerals to clays and iron (oxyhydr)oxides, and causing gains and losses in several chemical elements (e.g., Al, Fe, Mg; Caillaud et al., 2006, 2009; Destrigneville et al., 1998; Karpoff et al., 1989, 2017; Snow and Dick, 1995; Venturelli et al., 1997)

In this study, we investigate mass transfer in major and trace elements occurring during serpentinization of peridotites from the ultraslow-spreading South West Indian Ridge (SWIR), and more particularly from the “smooth seafloor areas”. Interest on this particular smooth seafloor area is related to: 1) their near orthogonal geometry to the ridge axis, allowing to evaluate the influence of serpentinization with increasing distance from the ridge and the role of detachment faulting, and 2) the opportunity to determine, by comparing geochemical data between smooth seafloor and MAR serpentinites, the influence of magmatic regime on fluid-rock interactions and chemical budget of the oceanic lithosphere. This paper will hence focus on presenting and discussing major and trace elements compositions of the smooth seafloor serpentinites to shed light on the consequences of fluid-rock interactions during long-lived exhumation and hydration history.

2. Geological context

The South West Indian Ridge is an ultraslow-spreading ridge (14 mm/yr; Patriat et al., 1997) located in the Indian Ocean, between the Bouvet Triple Junction in the SW and the Rodrigues Triple Junction (RTJ) in the NE (Fig. 1). Between the Indomed Transform Fault (TF) and the RTJ, the SWIR is divided by four major transform faults (Discovery II, Gallieni, Atlantis II and Melville) and shows from west to east : 1) a decrease in magmatic activity, as suggested by an increase in axial valley depth (3 km in the west to 4.7 km in the east; Cannat et al., 1999) and 2) a decrease in oceanic crust thickness (6.7 km to the west and 2.4 km to the east; Muller et al., 1997). This longitudinal evolution is due to an unusually cold mantle under the easternmost part of the SWIR (Debayle and Lévêque, 1997) and the thermal influence of the Crozet hotspot to the westernmost part (Sauter et al., 2009). The SWIR mantle has a heterogeneous chemical and isotopic composition (Dupré and Allègre, 1983) and is believed to contain exotic components, such as pieces of ancient continental crust, pyroxenites or eclogites (Gautheron et al., 2015; Salters and Dick, 2002).

The study area is located in the easternmost part of the SWIR, eastward of the Melville TF, between 62° and 65°E (Fig. 1). This zone is divided in two portions with different spreading trends and rates: the eastern part of the ridge shows a nearly orthogonal spreading with an Extension Spreading Rate (ESR) of 7 mm/yr, while the western part of the area spreads slightly obliquely with an ESR of 6 mm/yr (Patriat et al., 1997). In the 62-65°E region, the oceanic seafloor is composed of three different seafloor morphologies related to magma supply: volcanic seafloor (high magma supply), corrugated seafloor (moderate magma supply) and the smooth seafloor (minimal melt supply; Cannat et al., 2006). Volcanic seafloor morphology and corrugated surfaces are commonly found along slow-spreading ridges, while smooth seafloor was, so far, only been observed in this region of the SWIR (Cannat et al., 2006). The smooth

seafloor represents 37% of the SWIR seafloor surface between 62° and 65°E (Cannat et al., 2006). It is shaped as 15 to 30 km-long corridors, almost perpendicular to the ridge axis (Fig. 1; Cannat et al., 2006; Sauter et al., 2013), and is characterized by a predominance of mantle peridotites (96%) with a very low proportion of mafic rocks (<3% of the dredged volume). Its formation is related to nearly amagmatic conditions and mainly dominated by tectonic processes (Cannat et al., 1999, 2006; Sauter et al., 2013).

In the 62-65°E region, mineralogical and chemical compositions of the abyssal peridotites and basaltic rocks are particular. Indeed, clinopyroxenes are characterized by high Na_2O and low TiO_2 contents, compared to those of MAR peridotites, indicating metasomatic interaction (Seyler et al., 2003). Low CaO and Al_2O_3 contents together with high $Na_{8.0}$ and Sr contents of basaltic glasses suggest that one or more early episodes of mantle partial melting occurred followed by significant melt-rock interactions (Meyzen et al., 2003; Paquet et al., 2016). Alteration of the smooth seafloor peridotites have been firstly investigated by Rouméjon and Cannat (2014) and Rouméjon et al. (2015) with the aim to better understand the petrographic textures and the fluid pathways of exhumed serpentinites in such peculiar geologic setting.

3. Methods

The serpentinites investigated in this study were sampled during the SMOOTHSEAFLOOR (SMS) expedition in 2010 (R.V. Marion Dufresne, cruise MD183, PI: D. Sauter and M. Cannat). During this cruise, thirty-three dredges were conducted on and off axis of the SWIR along the two N-S-oriented zones of smooth seafloor, between the magnetic anomalies C5n.o at north and C3An.y at south (Fig. 1; Sauter et al., 2013). The recovered samples consisted of variously serpentinized and oxidized peridotites, with minor gabbros and basaltic rocks (Sauter et al., 2013). In this study, mineralogical and geochemical compositions of a selection of thirty-

115 one serpentinite samples collected from the western and eastern corridors (Fig. 1) were carried
116 out in order to assess changes in redox conditions and to better understand and evaluate
117 exchanges in chemical elements during long-lived history of fluid-rock interactions.

118 Petrographic observations of 31 thin sections of serpentinites allows to determine the
119 primary and secondary mineral assemblages and the different serpentinization textures.
120 Protolith, primary and secondary mineral assemblages, serpentinization degree and textures are
121 presented in Table 1. Distance from the ridge was recalculated for each sample using the mean
122 position of the dredge given in Sauter et al. (2013; Fig. 1 and supplementray material). First
123 number of sample label corresponds to the dredge number; therefore, samples collected from
124 the same dredge would have similar distance from the ridge. Complementary mineral
125 identifications were performed by X-Ray Diffraction (XRD) and Raman spectroscopy to
126 determine the different serpentine types and the eventual occurrences of other phyllosilicates
127 (e.g., clays, talc). XRD patterns were recorded on a Brucker D8 diffractometer at Géosciences
128 Environnement Toulouse (GET, France) with copper anode using the CuKα radiation at
129 1.54060 nm (40 kV, 40 mA) and LinxEye detector. For each sample, XRD patterns were first
130 recorded on non-oriented bulk rock powder to investigate the presence of phyllosilicates (e.g.
131 serpentine, smectites). Non-oriented patterns were acquired over a 2-80° 2θ range with a step
132 size of 0.02° 2θ and 1s per step. Then the finest fraction (<2 µm) of each sample was separated
133 and prepared as three oriented sections: air-dried, saturated with ethylene glycol (EG) and
134 heated at 500°C (Appendix A). Oriented patterns were acquired over a 2-36° 2θ range with a
135 step size of 0.02° 2θ and 1s per step. Raman spectroscopic analyses were performed on
136 serpentine minerals of six particular samples (Table 1) at the Laboratoire de Géologie de Lyon
137 (ENS Lyon, France) with a confocal Horiba Jobin-Yvon LabRam HR800 spectrometer. The
138 used light source was an argon-ion laser at 514.5 nm wavelength and a power of 6 mW on
139 silicate minerals. The measurements were performed between 150 and 1200 cm^{-1} and between

140 3600 and 3800 cm^{-1} to observe respectively the vibrational frequencies of Si-groups and OH-
141 groups (Appendix A).

142 Chemical compositions of primary and secondary minerals were obtained using a CAMECA
143 SX100 Electron Microprobe, equipped with four WDS spectrometers and twelve diffraction
144 crystals at the Laboratoire Magmas et Volcans (LMV), Clermont-Ferrand (France). Minerals
145 were analyzed under a 15 kV tension and a 15 nA beam current, with a 5 µm spot size and a
146 counting time of 10 s. In situ mineral compositions of the studied serpentinites are presented in
147 Appendix B.

148 Bulk rock major and trace element compositions were carried out on 31 serpentinites and
149 are presented in Table 2. Major elements were measured by Inductively Coupled Plasma-
150 Optical Emission Spectrometry (ICP-OES) on a Thermo Fisher iCAP 6500 at SARM
151 commercial laboratory (CRPG, Nancy, France). Additional potentiometric titration with
152 potassium dichromate after dissolution of the sample in HF/H_2SO_4 mixture was performed on
153 all serpentinites to obtain FeO contents and to calculate Fe^{3+}/Fe_{tot} ratios (Maxwell, 1968;
154 Carignan et al., 2001). Bulk rock trace element concentrations were measured by an Inductively
155 Coupled Plasma-Mass Spectrometer (ICP-MS) on a quadrupole Agilent 7500 at LMV,
156 Clermont Ferrand (France), after acid digestion of the sample. The reproducibility of the trace
157 analyses, given as 2σ on 16 replicates of BCR-2 and BIR-1 USGS standards, is less than 2%
158 for most of the elements, except Ni (4%) and V (20%). Additional boron concentrations were
159 also measured at SARM (CRPG, Nancy, France) by UV-visible spectrophotometry after fusion
160 with Na_2CO_3. Errors are given with a 99% confidence interval for all elements.

161

162 **4. Results**

163

164 4.1. Petrographic description of the investigated serpentinites

The SMS serpentinites investigated in this study are mostly serpentinized harzburgites (20 samples), lherzolites (7 samples) and dunites (2 samples; Table 1). Two other samples (SMS 5-4-17 and SMS-26-2-11) showing a higher proportion in pyroxenes (~70%,) are thus classified as serpentinized olivine websterites. The serpentinization degree of the SMS serpentinites ranges from moderate (50%) to complete (100%; Table 1).

4.1.1. Primary mineralogy

Primary mineral assemblages of the variously serpentinized peridotites of the smooth seafloor area are constituted of olivine, pyroxenes (ortho- and clino-) and Cr-spinel. Olivine is present as relic mineral in the center of the serpentine mesh cells in the less serpentinized samples (Fig. 2A) and represents a maximum of 35% (modal proportion) of the whole rock. Relics are roundish to subhedral with a maximum size of 0.5 mm. Olivine composition ranges between Fo_{88} and Fo_{91}, with a Fo_{90} composition in average and a structural formula $Mg_{1.8}Fe_{0.2}SiO_4$, and a mean NiO content of 0.4 wt.% (Appendix B), similarly to other abyssal peridotites (Komor et al., 1990; Rouméjon and Cannat, 2014; Seyler et al., 2003; Snow and Dick, 1995).

Pyroxene relics are more abundant than olivine relics. No preferential orientation of the pyroxene grains was observed petrographically. However undulating extinction and kink-band deformations observed in some samples indicate high-temperature ductile deformation before serpentinization. Ortho- and clinopyroxenes were both identified in the serpentinized peridotites (Fig. 2A). Orthopyroxene is defined as enstatite, with $En_{88}Fs_{10}Wo_2$ as average composition (Appendix B), and frequently displays exsolution lamellae of augite ($En_{56}Fs_7Wo_{37}$ in average). Most of the orthopyroxenes from the SMS serpentinites have TiO_2 concentrations

higher than 0.1 wt.% (up to 0.21 wt.%), within the range of the orthopyroxenes of the SWIR peridotites (Frisby et al., 2016; Rouméjon and Cannat, 2014; Seyler et al., 2003; Snow and Dick, 1995), but higher than those of the MAR peridotites (Cannat et al., 1992; Kodolányi et al., 2012). Clinopyroxene is present as diopside, with an average composition $En_{46}Fs_5Wo_{49}$, and shows frequent exsolution lamellae of augite ($En_{56}Fs_7Wo_{37}$). Concentrations in Na_2O, Al_2O_3 and TiO_2 in clinopyroxene are higher than those measured in the MAR clinopyroxenes (> 0.11 wt.%, > 4.5 wt.%, > 0.2 wt.%, respectively).

Spinel in the SMS serpentinites is present either as fresh Cr-spinel or as its alteration phase called ferritchromite. Fresh Cr-spinel is homogeneous with a brown to mahogany color in plane light and with a structural formula being $(Fe^{2+}_{0.22-0.36}Mg^{2+}_{0.64-0.77})(Fe^{3+}_{0.01-0.1}Cr^{3+}_{0.18-0.54}Al^{3+}_{1.38-1.75})O_4$. Their Cr# (= Cr/(Cr+Al) x 100 in atomic proportion) varies between 9.4 and 28.3 (Appendix B), a range that overlaps the lower end of the SWIR Cr-spinels range (14.9 – 48.8; Dick and Bullen, 1984; Seyler et al., 2003) and that is significantly lower than those of the MAR Cr-spinels (21.4 – 74.2; Komor et al., 1990; Kodolányi et al., 2012; Cannat et al., 1992).

4.1.2. Secondary mineralogy

Secondary minerals being identified in the SMS serpentinites are serpentine, magnetite, tremolite, chlorite, talc, hydrogarnet, goethite, hematite, carbonates and sulfides. The most abundant secondary mineral present in the serpentinites and replacing both primary olivine and orthopyroxene is serpentine, which gives a pale green to grey-black color in handspecimen (Fig. 2B and 2C). Olivine is replaced by serpentine with a classical mesh texture, where the center of the mesh cells is either a relic of olivine or lizardite (for more advanced serpentinization stages). Mesh cells are up to 1 mm wide and are outlined by a network of thin magnetite veins (Fig. 2D). Mesh texture is predominant but ribbon texture is also observed, e.g. SMS 14-5-8,

17-4-2 and 30-2-2. Dark grey pseudomorphic bastite replaces orthopyroxene, either partially along the rim or totally and are commonly crosscut by numerous serpentine veins (Fig. 2B). RAMAN analyses on bastite pseudomorphs display a shift of the lizardite peaks (Appendix A), suggesting that a very small proportion of antigorite may be present with lizardite. However, antigorite remains unnoticeable on bulk rock XRD spectra. In most of the samples, serpentine was identified as lizardite 1T (XRD spectra, Appendix A). Antigorite is present only in the two olivine websterites (SMS 5-4-17 and 26-2-11) in replacement of pyroxenes, together with tremolite and chlorite (Fig. 2E and 2F). No brucite was detected on XRD or RAMAN spectra. Secondary veins of fibrous or banded serpentine, mostly chrysotile and lizardite, are abundant in SMS serpentinites and crosscut the preexistent mesh texture with a preferred orientation. Interlocking and interpenetrating recrystallization textures were only observed in two serpentinized harzburgites, SMS 15-3-16 and 29-5-41.

Serpentine chemical composition (irrespectively of varieties and textures) shows a wide range: SiO_2 ranges from 34.2 to 45.0 wt.%, MgO from 26.0 to 44.4 wt.%, FeO from 1.5 to 14.8 wt.% and Al_2O_3 up to 4.5 wt.% (Appendix B). Lizardite in the mesh texture has an average structural formula $(Fe_{0.2}Mg_{2.8})Si_2O_5(OH)_4$ and shows higher concentrations in FeO (> 10 wt.%) than bastite and serpentine veins. Antigorite is characterized by slightly higher content in Al_2O_3 as indicated by its formula $(Fe_{0.3}Mg_{2.7})(Si_{1.9}Al_{0.1})O_5(OH)_4$. Bastite frequently contains significant concentrations in CaO and Al_2O_3 (up to ~ 2 wt.%), as indicated by its structural formula $(Ca_{0\text{-}0.1}Fe_{0.1\text{-}0.4}Mg_{2.5\text{-}2.9})(Si_{1.8\text{-}2}Al_{0\text{-}0.2})O_5(OH)_4$. Serpentine in recrystallized textures is also slightly enriched in Al_2O_3 compared to that in mesh textures (up to 3.5 wt.%). Chrysotile veins have similar composition than lizardite in mesh textures and bastites. Na_2O and NiO concentrations are comparable for all serpentine textures (0-0.25 wt.% and 0-0.7 wt.%, respectively).

Magnetite ($Fe^{2+}Fe^{3+}{}_2O_3$) appears in three different habits in the SMS serpentinites. It occurs predominantly as veins forming a network underlining the serpentine mesh cells (Fig. 2B). Secondly, it is also found as alteration mineral of sulfides (pentlandite or millerite), forming a grey alteration corona around the yellow sulfide core in reflected light. In both cases, its composition is classical (Fe_2O_3 68 wt.%, FeO 31 wt.%). The magnetite is thirdly present as exsolution and along the rims and cracks of Cr-spinel grains, or as ferritchromite when Cr-spinel replacement is complete (when all Mg, Al and Cr are replaced by Fe; Kimball, 1990). Altered Cr-spinel composition is then modified, with lower concentrations in Cr_2O_3, MgO and Al_2O_3 than fresh Cr-spinel and a structural formula being $(Fe^{2+}{}_{0.30–0.83}Mg^{2+}{}_{0.13-0.70})(Fe^{3+}{}_{0.03–1.28}Cr^{3+}{}_{0.38–1.14}Al^{3+}{}_{0.33–1.34})O_4$.

Other secondary minerals include tremolite, talc, chlorite, and hydrogarnet. Tremolite, whose structural formula is $Ca_{1.9}Na_{0.1}Mg_{4.6}Fe_{0.3}(Al_{0.2}Si_{7.8}O_{22})(OH)_2$, is found as replacement of clinopyroxenes forming elongated or fan-shaped crystals. Tremolite veins are scarce, being only identified in two serpentinized harzburgites (SMS 5-4-14 and 27-2-19) and two olivine websterites (SMS 5-4-17 and 26-2-11). In SMS 5-4-17 and 26-2-11, tremolite is found in veins intertwined with antigorite and chlorite, while opaque iron oxides and hydroxides, together with serpentine, replace olivine (Fig. 2E and 2F). Talc $Mg_3Si_4O_{10}(OH)_2$ is found either as replacement of orthopyroxene or as veins in samples SMS 1-2-35, 4-2-1, 5-4-14, 10-5-6, 27-2-19 and 29-5-41 (>1% modal), indicating circulation of a Si-rich fluid. Four peridotites (SMS 1-2-35, 7-3-7, 22-6-13 and 34-2-17) display interstitial plagioclase that was totally replaced by hydrogarnet during fluid-rock interaction (Fig. 3A) suggesting magmatic impregnation. Hydrogarnet is present as clusters of very small dark crystals (10-15µm each; Fig. 3A). The replacement of plagioclase by hydrogarnet releases Al that is used to precipitate clinochlore (Appendix B) as alteration coronas around the hydrogarnet (Fig. 3A). Chlorite is also observed associated with and related to alteration of Cr-spinel around which it forms a dark blue corona

in cross-polarized light (Fig. 3A, Appendix B). Chlorite veins are only found in serpentinized olivine websterites SMS 5-4-17 and 26-2-11. Hydrogarnet and chlorite alteration shows clearly plagioclase impregnation in the peridotites, however, other petrographic evidences, such as inter-pyroxenes cusps boundaries (Fig. 3B) and/or olivine-pyroxenes interstitial crystallization textures (Table 1) suggest different degrees of melt-rock interactions (Piccardo et al., 2007; Rampone et al., 1997).

Sulfide minerals are very scarce and only represent a very tiny proportion of the bulk rock (<<1%). Some relics of euhedral to subhedral primary sulfides, whose size can reach up to 100 µm, occur predominantly as pentlandite $(Fe,Ni)_9S_8$. Secondary sulfides are sub-rounded or bleb-shaped, with a maximum size of 50 µm, and are mainly pentlandite and millerite (NiS). They frequently replace primary pentlandite in association with magnetite. The composition of pentlandite (primary and secondary) ranges between 32.7-35.5 wt.% S, 27.3-42.4 wt.% Fe, 21.4-37.1 wt.% Ni, 0.3-4 wt.% Co and 0-2.4 wt.% Cu, while millerite is composed of 59.6-72.3 wt.% Ni, 27-35.6 wt.% S, 1.4-4.2 wt.% Fe, 0-0.7 wt.% Co and 0-1.4 wt.% Cu. Two samples show distinct secondary sulfide mineral assemblages: SMS 2-2-11 displays an assemblage of millerite + violarite ($FeNi_2S_4$) + chalcopyrite ($CuFeS_2$), while SMS 5-4-14 contains awaruite (Ni_3Fe) associated to pentlandite. Awaruite generally forms during early stages of serpentinization when reducing conditions predominates (Delacour et al., 2008b; Frost, 1985). However, due to the high serpentinization degree of the sample (91%; Table 1), it is more likely that awaruite results from the destabilization of pentlandite (Chamberlain, 1965; Kanehira et al., 1975).

Nine SMS serpentinites contain significant proportions (>1% modal) of hematite (Fe_2O_3) and goethite (FeO(OH)) (Table 1). These Fe-minerals are precipitated as final product of complete sulfide alteration (e.g., SMS 4-2-1, 11-2-11, 14-5-8, 21-5-6), displaying then shapes, sizes and textures similar to those of their parent sulfide minerals (primary or secondary

289 pentlandite and millerite; Fig. 3C). They are also found as amorphous iron oxides and/or
290 hydroxides (named as IOH further in this manuscript, e.g., SMS 4-2-1, 5-4-14, 5-4-17, 11-2-
291 11, 14-5-1, 14-5-8, 21-5-6, 26-2-11, 33-3-27), which result from the combined alteration of
292 serpentine and magnetite (Caillaud et al., 2006; Venturelli et al., 1997). These IOH are reddish
293 to orange in reflected light and replace serpentine at the center of the mesh cells (Fig. 2E-F and
294 Fig. 3C-D). Although their absence of crystallinity prevented acquisition of reliable chemical
295 analyses, their identification was suggested by peaks of weak intensity on RAMAN spectra.
296 When the IOH are present in the serpentine mesh texture, magnetite is locally absent.
297 Carbonates are present as calcite ($CaCO_3$) in three samples. They either form dark brown
298 opaque areas with blurred limits in thin section (SMS 8-2-25) or veins of 1 µm to 1 mm (SMS
299 10-5-6 and 29-5-41). In sample SMS 10-5-6, calcite is associated with talc in large veins. One
300 occurrence of aragonite was identified by RAMAN spectroscopy on an isolated vein in SMS
301 34-2-17. Elementary and isotope carbon analyses (Total Inorganic Carbon >600 ppm,
302 $\delta^{13}C_{TIC}$ ~ +3‰; pers. data) suggest that two other samples (SMS 1-2-35 and 27-2-19) contains
303 little amounts of carbonates not visible in thin sections.
304
305 4.2. Bulk rock chemical composition of serpentinites
306
307 *4.2.1. Major elements*
308
309 Bulk rock major and trace elements compositions of 31 serpentinites are given in Table 2.
310 These serpentinites show a wide range of compositions: SiO_2 (non-anhydrous values) ranges
311 from 36.9 to 44.6 wt.% (average 40.1 wt.%), Al_2O_3 from 0.6 to 3.9 wt.% (av. 2.2 wt.%), Fe_2O_{3T}
312 from 7.2 to 19.6 wt.% (av. 9.2 wt.%), MgO from 25.8 to 37.9 wt.% (av. 34.3 wt.%), CaO from
313 0.2 to 6.1 wt.% (av. 2.3 wt.%), Na_2O from 0.1 to 0.8 wt.% (av. 0.2 wt.%) and LOI from 4.9 to

14.5 wt.% (av. 11.6 wt.%). These compositions are similar to those reported in previous studies on SWIR serpentinites (Niu, 2004; Rouméjon and Cannat, 2014). In a diagram MgO/SiO_2 vs. Al_2O_3/SiO_2 (Fig. 4), the studied serpentinites follow the terrestrial array defined by Jagoutz et al. (1979) and Hart and Zindler (1986) for mantle peridotites ($0.65 < MgO/SiO_2 < 1$ and $0.015 < Al_2O_3/SiO_2 < 0.09$). However, one serpentinized lherzolite (SMS 11-2-4) and four IOH-serpentinites (containing strictly ≥ 1% modal, SMS 4-2-1, 5-4-17, 11-2-11 and 33-3-27) show higher Al_2O_3/SiO_2 ratios and lower MgO/SiO_2 ratios than SWIR and MAR peridotites (Fig. 4; Niu, 2004; Paulick et al., 2006; Jöns et al., 2010; Kodolányi et al., 2012; Rouméjon, 2014; Rouméjon and Cannat, 2014).

The Fe^{3+}/Fe_{total} ratio, used as a proxy of oxidation degree of the serpentinites, ranges from 0.39 and 0.87. This ratio increases with both LOI and estimated visual serpentinization degree of the rock (Fig. 5). Serpentinites with low serpentinization degrees (~ 50%; e.g., SMS 1-2-1) have low Fe^{3+}/Fe_{total} ratios and LOI (~ 4 wt.%), whereas those with high serpentinization degrees (99 %; e.g., SMS 14-5-1) have high Fe^{3+}/Fe_{total} ratios and LOI (14 wt.%). IOH-serpentinites display high Fe^{3+}/Fe_{total} ratios, LOI and serpentinization degree (e.g., SMS 11-2-11, Fe^{3+}/Fe_{total} ratio of 0.87, 9.5 wt.% LOI).

4.2.2. Trace elements

Multi-element patterns of the SMS serpentinites, volatile-free and normalized to primitive mantle (Sun and McDonough, 1989), are mostly depleted compared to primitive mantle (PM; Fig. 6A), except one serpentinite showing petrographic evidences of plagioclase impregnation, SMS 22-6-13, which is enriched 2 to 300 times to the PM. Trace element spectra of SMS serpentinites are within the range of the SWIR serpentinites (Niu, 2004) but enriched in almost all trace elements compared to MAR serpentinites (Andreani et al., 2014; Deschamps et al.,

2013 and references within). LILE (Cs, Ba, Rb) concentrations and high positive anomalies in U, Pb and Sr (between 0.1 and 100 times the PM) of SMS serpentinites are similar to those of abyssal peridotites in the literature (Bodinier and Godard, 2008; Deschamps et al., 2013). Positive anomalies in U, Pb and Sr are common features in serpentinites, irrespectively of their context of formation (Deschamps et al., 2013). Rare Earth Elements (REE) patterns, volatile-free and normalized to chondrite (Fig. 6B; Sun and McDonough, 1989), show a general depletion in LREE and MREE (La to Eu) compared to the chondrite value (CV; Fig. 6B), with the exception of few samples, the serpentinite with plagioclase impregnation SMS 22-6-13 (enriched up to 38 times the CV) and five IOH- serpentinites, SMS 4-2-1, 11-2-11, 14-5-8, 5-4-17 and 33-3-27, which are enriched up to 10 times the CV. HREE (from Gd to Lu) concentrations show a wide range, from slightly depleted (minimum 0.12 × CV) to enriched (up to 14 × CV). Half of the SMS serpentinites show depletion in LREE compared to HREE (west corridor: SMS 1-2-1, 1-2-35, 2-2-11, 2-2-17, 3-2-1, 6-3-14, 7-3-7, 8-2-17, 8-2-25, 10-5-6, 11-2-4, 15-3-16, 17-4-19, 17-4-32; east corridor: SMS 27-2-19, 28-4-10, 29-6-13), whereas the other half (west corridor: SMS 4-2-1, 5-4-14, 5-4-17, 11-2-11, 13-4-11, 14-5-1, 14-5-8; east corridor: SMS 21-5-6, 22-6-13, 29-5-41, 30-2-2, 33-3-27, 34-2-17) show enrichment in both LREE and HREE (Fig. 6B). Twenty-one samples (except SMS 1-2-35, 6-3-14, 8-2-17, 8-2-25, 10-5-6, 17-4-19, 17-4-32, 27-2-19, 28-4-10, 29-6-13 and 30-2-2) show a Ce anomaly, which is negative for most of the serpentinites (0.004 to 1.56 × CV; e.g., SMS 11-2-11) and only positive for two serpentinites (0.7 to 128 × CV, SMS 22-6-13 and 29-5-41; Fig. 6B). By comparison, such Ce anomaly is not observed in MAR serpentinites (Fig. 6B). In addition, SMS serpentinites lack Eu anomaly (Fig. 6B). The SMS serpentinites also contain higher concentrations in Fluid Mobile Elements (FME) than the PM: B (33-115 ppm, average 65 ppm), Li (0.94-8.83 ppm, av. 4.45 ppm), Cd (0.02-0.17 ppm, av. 0.06 ppm), As (0.22-28 ppm, av. 3.62 ppm), and Sb

(0.003-9.49 ppm, av. 1.03 ppm) (Table 2). These values are within the range of global abyssal serpentinites (Niu, 2004; Deschamps et al., 2013 and references within).

5. Discussion

Since its formation at and along the ridge axis, via magmatic or tectonic-dominated processes, the oceanic lithosphere is affected by interaction with seawater-derived, magmatic or hydrothermal fluids resulting in chemical exchanges between the rocks and the fluids. Quantifying these chemical transfers and understanding in which conditions they occur are crucial to better constrain the biogeochemical cycles of the Earth and the compositions of the different reservoirs. The smooth seafloor areas along the SWIR, sites investigated during this study, have the particularity to be nearly amagmatic and to be formed by tectonically-dominated processes ("flip-flop model"; Sauter et al., 2013). Consequently, fluid interaction in these zones will affect predominantly the ultramafic rocks exposed on the ocean floor via detachment faulting. In the following section, we will discuss the influence of long-lived interaction of ultramafic rocks with fluids (magmatic, hydrothermal, seawater, …) on chemical compositions of the rocks and on chemical transfers with a focus on some specific tracers and elements. In order to evaluate the effect of time and the lateral variability in such specific ultraslow-spreading context, chemical compositions will be regarded as a function of ridge axis distance and thus of exhumation history.

5.1. Influence of magmatic processes on protolith compositions

Primary compositions of serpentinites protoliths at the smoothseafloor, i.e., harzburgites, lherzolites, dunites or olivine websterites, result from magmatic processes, such as partial

388 melting and melt-rock interaction (i.e. impregnation, refertilization) and depend on underlying
389 mantle composition. Knowing precisely these primary compositions is important to evaluate
390 element mass transfer occurring during secondary fluid-rock interaction within the oceanic
391 lithosphere.
392
393 *5.1.1. Partial melting influence on protolith composition*
394
395 In order to differentiate between primary and secondary element mass transfer, it is crucial
396 to evaluate what element are mobile or immobile and how they evolve during primary and
397 secondary processes. During magmatic processes, partial melting degree and element
398 compatibility and mobility significantly impact the chemical composition of the protolith.
399 Partial melting degree in mantle-derived rocks is commonly evaluated using TiO_2 content of
400 the rocks, as this element is considered as immobile during hydrothermal alteration processes
401 (Finlow-Bates and Stumpfl, 1981; Deschamps et al., 2013). Therefore, any major element
402 correlating with TiO_2 content would then reflect the protolith composition of the SMS
403 serpentinites. During oceanic upper mantle partial melting, as partial melting degree increases,
404 SiO_2, CaO, Na_2O, Al_2O_3 and TiO_2 contents will progressively decrease in residual peridotites
405 whereas MgO and Fe_2O_3 contents will increase (Bodinier and Godard, 2003; Niu et al., 1997).
406 This evolution of TiO_2 with partial melting degree is shown in Figure 7 for the studied SMS
407 serpentinized peridotites: the serpentinized dunites show the lowest TiO_2 contents (<
408 0.02 wt.%), the serpentinized lherzolites have the highest TiO_2 contents (> 0.06 wt.%), and the
409 serpentinized harzburgites display intermediate values between 0.02 and 0.08 wt.%. The only
410 exception to these subgroups is the Ti-enriched serpentinized harzburgite, SMS 22-6-13, which
411 shows a high TiO_2 content ~0.16 wt.%. This enrichment in TiO_2 content for this specific sample
412 will be discussed in section 5.1.2.

Among major elements, Al_2O_3 is classically considered, similarly to TiO_2, as immobile during fluid-rock interaction (Sinha et al., 1986), except in very alkaline conditions (Shervais et al., 2005). Both MgO and CaO are commonly lost to the fluids (Coleman and Keith, 1971; Kelley et al., 2001; Snow and Dick, 1995), while studies on SiO_2, Fe_2O_3 and Na_2O behavior are limited or not fully conclusive (Malvoisin, 2015; Shervais et al., 2005; Sinha et al., 1986). In the SMS serpentinites, Al_2O_3 content exclusively results from magmatic processes, as it fully correlates with TiO_2 content (Fig. 7). It is worthwhile to note that Al_2O_3 contents in SMS serpentinites are within the range of the SWIR peridotites but higher than that of the MAR serpentinites (Fig. 4 et 7). This suggests that the depleted upper mantle of the SWIR would be initially enriched in Al_2O_3 compared to the upper mantle of the MAR. Similar to Al_2O_3, CaO content correlates with TiO_2 content (Fig. 7), the highest contents being related to the occurrences of clinopyroxenes in the serpentinized lherzolites. Only two samples, SMS 10-5-6 and 29-5-41, are off the trend with higher CaO contents (respectively 6.1 and 2 wt% non-anhydrous). This enrichment is related to the presence of calcite veins in the serpentinites that precipitated from the combination of Ca and marine dissolved inorganic carbon (Dessimoulie, pers. data), similarly to other places along mid-oceanic ridges (Kelley et al., 2001, 2005; Delacour et al., 2008a; Schwarzenbach et al., 2013). The other major elements, SiO_2, MgO, Fe_2O_{3T} and Na_2O, display rough correlation with TiO_2 content (Fig. 7): constant for Fe_2O_{3T} and SiO_2, negative for MgO and positive for Na_2O, these trends resulting from mantle partial melting (Bodinier and Godard, 2003). However, some discrepancies occur in those correlations, in particular for IOH-serpentinites that spread out from the trend defined by the other serpentinites, showing lower MgO content and higher Fe_2O_3 and Na_2O contents. These peculiar compositions likely reflect mobility of these three elements during fluid-rock interactions (see discussion section 5.2).

REE patterns of the serpentinites can also provide information on magmatic processes and on partial melting degree. In this study, the subparallel HREE patterns of the SMS serpentinized peridotites (Fig. 6B) indicate different partial melting degrees of a mantle source (Bodinier and Godard, 2003). HREE contents of SMS serpentinites are thus representative of the protolith composition. In contrast, overlapping occurs for LREE suggesting that concentration in these LREE were subsequently modified by later processes, i.e., melt-rock or fluid-rock interactions.

5.1.2. Melt-rock interaction influence on protolith composition

At mid-oceanic ridges, peridotites are commonly percolated by ascending basaltic melts that can modify their bulk rock composition, depending on the melt composition and the degree of melt-rock interaction (Niu, 2004; Niu et al., 1997; Piccardo et al., 2007; Rampone et al., 1997). Melt-rock interactions and/or impregnation processes, if not cryptic, lead to changes in major and trace element compositions, as well as several petrographic evidences (e.g., plagioclase impregnation, REE flat patterns, enrichment in Fe, Ti, Na, …). Abyssal peridotites are residues of partial melting and then depleted in REE compared to the primitive mantle (PM). Thus any REE spectra enriched compared to the PM value could result from refertilization processes (Bodinier and Godard, 2003; Deschamps et al., 2013; Niu, 2004). In addition, impregnation of peridotites by basaltic melts, which are enriched in both LREE and HREE, produces flat to enriched REE patterns (Bodinier and Godard, 2003; Deschamps et al., 2013; Frisby et al., 2016). In case of cryptic metasomatism, REE spectra show a sigmoidal shape with higher enrichment in LREE than in HREE (Bodinier and Godard, 2003). Positive europium anomaly in the REE spectra of the peridotites could also be related to crystallization of plagioclase from percolating melts in the peridotites (Borghini and Rampone, 2007; Frisby et al., 2016; Paquet et al., 2016). High TiO_2 content in SWIR peridotites were interpreted as related to post-

462 melting/refertilization processes (Niu, 2004; Paquet et al., 2016; Warren and Shimizu, 2010)
463 whereas Seyler et al. (2003) suggested that this TiO_2 enrichment, together with Na_2O
464 enrichment, is rather due to a very heterogeneous Ti-enriched mantle source.

465 Some SMS peridotites show peculiar mineral assemblages and textures (e.g.,
466 olivine/pyroxene crystallization, interstitial plagioclase; see Table 1 and Fig. 3A et B) and/or
467 specific trace element compositions indicative of melt-rock reactions. Indeed, several
468 serpentinized abyssal peridotites are characterized by LREE-enriched and flat REE patterns
469 (e.g., SMS 22-6-13, SMS 11-2-11), while most of them show classical depletion in LREE
470 compared to HREE (Fig. 6B; Frisby et al., 2016; Niu, 2004). This enrichment is likely related
471 to melt-rock interaction as petrographic evidences of melt circulation were observed (e.g. SMS
472 11-2-4). One serpentinite, SMS 22-6-13, displays anomalously high trace element
473 concentrations, flat REE pattern (Fig. 6) and high TiO_2 concentrations (Fig. 7) implying thus
474 significant refertilization during melt circulation. Enrichment in REE is also observed for some
475 serpentinites containing high proportion of IOH (e.g., SMS 4-2-1, 11-2-11 and 33-3-27; Fig. 6)
476 suggesting that such enrichment is likely due to secondary processes such as fluid-rock
477 interaction. This will be discussed in Section 5.2.

478 Serpentinized peridotites characterized by olivine or pyroxene (re)crystallization (Fig. 3B)
479 do not show specific trace element compositions. This could be explained by percolation of a
480 melt in equilibrium with the peridotite (Bodinier and Godard, 2003) or by a little amount of
481 melt that would not affect the peridotite composition at the hand-specimen scale (Paquet et al.,
482 2016). The absence of Eu anomaly in samples with plagioclase impregnation (SMS 1-2-35 and
483 7-3-7) is likely related to alteration of plagioclase to hydrogarnet. Trace elements of previously
484 analyzed rodingites (i.e., plagioclase-bearing rocks altered to prehnite and grossular) display no
485 or negative Eu-anomaly, implying a leaching of Eu during the replacement of plagioclase (Tang
486 et al., 2018).

5.2. Influence of fluid-rock interactions on element mass transfer

Fluid-rock interaction affecting the oceanic lithosphere comprises a variety of processes depending on fluid fluxes, temperature and redox conditions. Along fast-spreading ridges, fluid-rock interactions are classically subdivided in high-temperature fluid-rock interaction, with formation of a hydrothermal system, and low-temperature fluid-rock interaction that are long-lasting processes that significantly affect the oceanic lithosphere composition (Alt, 2004; Von Herzen, 2004). For slow-spreading ridge, similar evolution was reported as detachment fault exhume ultramafic rocks with variable amounts of mafic rocks (i.e. gabbros; McCaig et al., 2007, 2010). In the following section, we present the consequences of fluid-rock interaction, with variable P-T, redox conditions and fluid compositions, on mass element transfer as a function of ridge distance, so with aging and exposure of ultramafic rocks on the ocean floor in an ultraslow-spreading context.

5.2.1. High-temperature fluid circulation

High-temperature fluid circulation in detachment-related context were reported along slow-spreading ridges to explain occurrences of high-temperature hydrothermal systems on ultramafic rocks exposed via detachment faulting (McCaig et al., 2007, 2010; Alt et al., 2013). In such settings, high-temperature fluid circulation, initiated by interaction of fluids with gabbro intrusions, affects the ultramafic rocks at depth. Evidences of such high-temperature fluid circulation, leading to the formation of sulfide deposits, either on the ocean floor or at depth within the oceanic lithosphere, were observed in some serpentinites of the SWIR smooth seafloor area. Indeed, three IOH-serpentinites, SMS 4-2-1, 5-4-17 and 11-2-11, have Fe_2O_{3T}

512 contents higher than other SMS serpentinites (>12 wt.%; Fig. 7), suggesting interaction of the
513 peridotites with high-temperature Fe-rich fluids. Interaction with such fluids (i.e., black
514 smoker-type fluids; Douville et al., 2002) also commonly lead to enrichments in S, precipitated
515 as sulfide minerals, REE and metals in the serpentinites. Enrichments in REE, FME and Cu,
516 Co and Zn characterized the three IOH-serpentinites (Fig. 6 and 11, Table 2). However, they
517 do not contain any sulfide, hematite and goethite only being present. A first possible
518 explanation of this lack of sulfide would be related to the long-lasted interaction of these
519 serpentinites with seawater or seawater-derived fluids that led to oxidation and desulfurization
520 of the sulfides (Delacour et al., 2008a; Karthe et al., 1993; Legrand et al., 2005; Richardson and
521 Vaughan, 1989). Another explanation for this lack of sulfides would be due to the circulation
522 of Cl-rich fluids, such as high-temperature hypersaline brines, which would provide an efficient
523 ligand to Fe and would favor precipitation of Fe-oxides over sulfides (Barton and Johnson,
524 2000). Further analyses of Cl and S contents and sulfur isotopes compositions of the SMS
525 serpentinites would help to better constrain the processes and formulate further interpretations.
526 Currently, the three IOH-serpentinites were collected at the most remote distance from the ridge
527 (> 40 km; Table 1), implying that interaction with high-temperature hydrothermal fluids
528 occurred, most likely at depth, during the early stages of spreading and detachment faulting.
529
530 *5.2.2. Evolution of fluid-rock interaction with distance from the ridge*
531
532 In order to evaluate which elements were influenced by long-lived fluid-rock interaction in
533 the specific setting of smooth seafloor along an ultra-slow spreading ridge, profiles with
534 distance from the ridge of serpentinization and oxidation degrees for serpentinites of both
535 western and eastern corridors of the smooth seafloor area were considered (Fig. 8). In these
536 profiles, Fe^{3+}/Fe_{total} ratio of the SMS serpentinites was used as proxy of serpentinization and

oxidation degrees, as this ratio is correlated to both visual serpentinization degree and LOI (Fig. 5; Evans, 2008; Andreani et al., 2013). In the west corridor, Fe^{3+}/Fe_{total} ratio of SMS serpentinites clearly increases with the distance from the ridge. Serpentinites sampled at a distance less than 5 km from the axis have a Fe^{3+}/Fe_{total} ratio around 0.4 (e.g., SMS 17-4-32 at 2.42 km with a Fe^{3+}/Fe_{total} ratio of 0.41; Tables 1 and **Error! Reference source not found.**), while serpentinites collected at a distance further than 40 km have Fe^{3+}/Fe_{total} ratio more than 0.8 (e.g., SMS 4-2-1 at 55.7 km, Fe^{3+}/Fe_{total} ratio of 0.81; Tables 1 and **Error! Reference source not found.** and Fig. 8), indicating then that distance profile from the ridge in the west corridor can be confidently used as serpentinization profiles. However, increase in Fe^{3+}/Fe_{total} ratio with distance of the ridge axis is not observed in the east corridor, the Fe^{3+}/Fe_{total} ratios ranging between 0.7 and 0.8 (Fig. 8). This difference between the two corridors is mainly related to the volcanic nature of the seafloor and/or a sampling bias of this study. Indeed, dredging of the southern part of the east corridor recovered mainly basaltic rocks, with few serpentinites samples, apart from dredges 22 and 25 located close to the C3An.y (Fig. 1). This scarcity in ultramafic rocks is linked to fewer detachment faults in the eastern corridor as identified in Sauter et al. (2013). For these reasons, evaluation of chemical transfers during serpentinization with time and distance of the ridge axis will only be carried out on the western smooth seafloor corridor.

5.2.3. Long-term serpentinization

Mass transfers of chemical, major and trace, elements during serpentinization were previously investigated by several authors without reaching to a consensus on the behavior of some elements. Indeed, behavior of major elements are a matter of debate (e.g., Coleman and Keith, 1971; Malvoisin, 2015; Mével, 2003; O'Hanley, 1996; Shervais et al., 2005; Snow and

562 Dick, 1995), due to the difficulty to access both serpentinites and their corresponding fresh
563 protolith, to the chemical heterogeneity of the peridotite protolith related to magmatic and post-
564 magmatic processes and to the long-lived fluid-rock interactions that affect peridotite protolith
565 and for which P-T and redox conditions and fluid compositions can be variable. In the particular
566 smooth seafloor context, evaluation of major and trace elements concentrations versus a
567 distance profile from the ridge, and the comparison of these concentrations to those of MAR
568 and SWIR serpentinites (Fig. 9), provide new insights on mass transfer during long-term
569 serpentinization.
570
571 5.2.3.1. Influence of long-term serpentinization on major elements
572
573 Behavior of Al_2O_3 and CaO concentrations in the SMS serpentinites was previously
574 discussed in Section 5.1.1. as these elements are inherited from the protolith (Fig. 7). The
575 absence of correlation of Al_2O_3 and TiO_2 contents with distance from the ridge (Fig. 9) indicate
576 that partial melting degree does not vary linearly through extension of the smooth seafloor, and
577 therefore that distance profiles confidently represent serpentinization profiles. Concentrations
578 in other major elements, Fe_2O_{3T}, MgO, SiO_2, Na_2O do not significantly increase or decrease
579 with the distance from the ridge (Fig. 9) suggesting that behavior of these elements is not
580 affected by serpentinization progress. Nevertheless, scattering in these elements with TiO_2 (Fig.
581 7) may be likely related to fluid-rock interaction processes.
582 Mg is known to be mobile during fluid-rock interaction, some studies having reported a loss
583 in Mg during serpentinization related to dissolution of brucite (Snow and Dick, 1995;
584 Malvoisin, 2015). Similar loss could be evoked to explain the low MgO contents in some SMS
585 serpentinites compared to the range of the SWIR and MAR abyssal peridotites (Fig. 4) and its
586 broad correlation with TiO_2 (Fig. 7). Behavior of Fe is closely related to Mg mobility, as these

two elements have close ionic radius and similar charge. Indeed, Fe/Mg ratio of most of the SMS serpentinites is well correlated to TiO_2 (Fig. 7), with the exception of the IOH-serpentinites that will be discussed in Section 5.2.4. This indicates that serpentinization does not significantly affect the mobility and thus the budget of MgO.

SiO_2 gains during serpentinization has been suggested by Malvoisin (2015), as an alternative explanation to low MgO/SiO_2 ratios of serpentinites (Fig. 4). However, no gain is observed for the SMS serpentinites as a function of distance from the ridge (Fig. 9). In addition, the presence of talc veins in some serpentinites (e.g., SMS 10-5-6, Table 1), related to the circulation and precipitation of Si-rich fluids, is not correlated with a gain in SiO_2. This suggests that SiO_2 concentrations variations are related to variations in MgO and FeO concentrations.

Scattering of Na_2O with TiO_2 and as a function of ridge distance is probably due to interaction of the SMS serpentinites with NaCl-rich fluids, i.e. seawater (~1 wt.% of Na; Quinby-Hunt and Turekian, 1983) and the precipitation of halite salts in serpentinites. These salts were however not observed petrographically. Quantification of bulk rock Cl concentrations in the serpentinites are necessary to unravel the origin of this scattering in Na_2O and if, similarly to previous studies (Sharp and Barnes, 2004), serpentinites of the smooth seafloor are enriched in Cl.

5.2.3.2. Influence of long-term serpentinization on Rare Earth Elements (REE)

Rare Earth Elements (REE) are commonly considered as immobile elements and their concentrations and distributions, shown by their spectrum shape on normalized diagrams, are commonly used to evidence magmatic and melt-rock interaction processes (Bodinier and Godard, 2003; Deschamps et al., 2013; Niu, 2004). However, recent studies reported REE mobility during fluid-rock interaction, expressed as an increase in REE concentrations with

advanced degrees of alteration (Andreani et al., 2014; Frisby et al., 2016, 2019; Niu, 2004; Paulick et al., 2006). Serpentinites from the west corridor show REE patterns similar to previously published studies on SWIR serpentinites but enriched compared to MAR serpentinites (Fig. 6B). While this enrichment in REE can be related to different magmatic regimes or melt-rock interaction via refertilization processes (see section 5.1.), some specific REE distribution and/or anomaly more likely result from secondary fluid-rock interaction processes. Indeed, the SWIR serpentinites show a Ce anomaly but no Eu anomaly in comparison to the MAR serpentinites (Fig. 6; Frisby et al., 2016; Niu, 2004; Rouméjon, 2014). These differences are related to fluid-rock interaction subsequently to accretion modes. Indeed, along the MAR, phases of magmatic activity alternate with phases of tectonic activity that allow exhumation of mafic and ultramafic rocks on the seafloor. Interaction of seawater-derived fluids with these mafic rocks is known to produce hydrothermal fluids with a positive Eu anomaly due to the occurrence of plagioclase in the mafic rocks (Douville et al., 2002). Some MAR serpentinites are thus thought to result from interaction with such evolved hydrothermal fluids (Deschamps et al., 2013). In the smooth seafloor context, mafic rocks are very scarce (Fig. 1; Cannat et al., 2006; Sauter et al., 2013), limiting then interaction with mafic rocks and thus enhancing interaction of peridotites with seawater or seawater-derived hydrothermal fluids whose chemical compositions are consequently different from those of the MAR.

Negative anomaly in Ce on REE spectra of serpentinites attests to interaction of peridotites with seawater under oxidizing conditions. However, the Ce/Ce* ratio does not show a clear evolution with distance from the ridge (Fig. 10) and thus as serpentinization degree increases. Nevertheless, two other LREE, La and Pr, show a clear increase in concentration with distance from the ridge (Fig. 10) indicating thus a progressive enrichment in these two elements with serpentinization progress, as already suggested by Frisby et al. (2016) for SWIR serpentinites.

637 Fluid Mobile Elements (FME; As, B, Ba, Cd, Li, Pb, Sb, Sr, and U) are, as indicated by their
638 names, mobile in the fluid phase and therefore during serpentinization of peridotites. Previous
639 studies demonstrated that serpentine minerals are enriched in FME (e.g., Boschi et al., 2008;
640 Decitre et al., 2003; Vils et al., 2008; Deschamps et al., 2013 and reference therein) which are
641 then transferred into subduction zone (Deschamps et al., 2011, 2013; Vils et al., 2011).
642 However, few studies investigated the increase of these elements as a function of
643 serpentinization progress and more particularly for long-lived serpentinization context such as
644 the smoothseafloor of the SWIR.
645 In the SMS serpentinites, Li and B are the only two FME whose concentration increases
646 with the serpentinization degree and with the distance from the ridge (Fig. 11). Boron
647 enrichment is a classical feature of altered oceanic crust (Spivack and Edmond, 1987) and
648 serpentinized peridotites (Boschi et al., 2008; Seyfried and Dibble, 1979; Vils et al., 2008). In
649 serpentinites, this enrichment is related to the incorporation of B from seawater (4.5 ppm,
650 Quinby-Hunt and Turekian, 1983) into serpentine (0.2-20 ppm; Boschi et al., 2008; Deschamps
651 et al., 2011) leading to bulk B concentrations up to 239 ppm (Boschi et al., 2008; Deschamps
652 et al., 2011; Seyfried and Dibble, 1979). Lithium is also classically enriched in serpentinites
653 (up to 1.37 ppm, Decitre et al., 2002; Deschamps et al., 2011; Lee et al., 2008; Niu, 2004; Vils
654 et al., 2008), but in contrast to B, serpentine minerals show very variable Li contents (0.20-
655 26.1 ppm), which are either enriched or depleted compared to primary minerals (Decitre et al.,
656 2002; Deschamps et al., 2011; Lee et al., 2008; Vils et al., 2008). Enrichments in Li and B in
657 SMS serpentinites (Fig. 11) are, as suggested in earlier studies, due to their incorporation into
658 serpentine phases as serpentinization progress. Only one serpentine (SMS 5-4-17) does not
659 show such enrichment, its Li concentration being low compared to its position from the ridge
660 (Fig. 11). This low Li concentration can be likely explained by the high temperature of the
661 serpentinizing fluid (>350°C), as indicated by its uncommon high modal proportions in chlorite

662 + tremolite + antigorite. Indeed, precipitation of this mineral assemblage is rather favorable to
663 Li leaching, as already observed during alteration of basalts (Seyfried et al., 1984). Similarly to
664 Fe^{3+}/Fe_{tot} ratio, B and Li concentrations of serpentinites could then be used as proxies of the
665 serpentinization degree. However, care must be taken for high temperature serpentinization and
666 for recrystallization of lizardite and chrysotile to antigorite, these two processes leading to a
667 release of Li and B (Deschamps et al., 2012; Kodolányi and Pettke, 2011; Ishikawa and
668 Nakamura, 1992; Seyfried et al., 1984).

669 Previous studies showed that both As and Sb are stored in serpentine minerals (Deschamps
670 et al., 2011; 2012; 2013), and that these enrichments are mainly related to circulation of a
671 sediment-derived fluid rich in Sb and As (Deschamps et al., 2012). While SMS serpentinites
672 are within the range of the previously published data for both elements (50 ppb to 22 ppm,
673 (Andreani et al., 2014; Paulick et al., 2006), it is difficult to evoke similar process to explain
674 this enrichment. Indeed, little sedimentary cover has been imaged on the outcropping mantle
675 rocks and volcanic seafloor (Supplementary data of Sauter et al., 2013). In addition, the
676 correlation between As and Sb with distance from the ridge axis (Fig. 11) would rather reflect
677 an enrichment with serpentinization degree, as interaction with sediment-derived fluid would
678 have produce scattering in the concentrations. Cadmium was not investigated in serpentinites
679 so far, but its behavior looks similar to those of Sb and As (Fig. 11). Enrichments in these
680 elements is favored for serpentinization processes at temperatures <300°C (Deschamps et al.,
681 2011). As conclusion, As, Sb, and Cd concentrations could also be used, similarly to LREE, as
682 serpentinization proxies.

683

684 5.2.4. Late oxidative alteration

685

686 Serpentinites from the smooth seafloor that experienced low-temperature serpentinization
687 are enriched in several elements and their enrichment is proportional to the serpentinization
688 degree and to the distance from the ridge. In contrast, IOH- serpentinites, while following the
689 overall enrichment tendencies, show higher Fe^{3+}/Fe_{tot} ratios (Fig. 5), Fe_2O_{3T}, Na_2O (Fig. 7),
690 LREE and FME contents (Fig. 10 and 11), suggesting that other processes, such as late
691 oxidative alteration, affected these IOH- serpentinites after long-term serpentinization.
692 Late oxidative alteration in these IOH-serpentinites is evidenced by the presence of both
693 hematite and goethite that leads to high Fe^{3+}/Fe_{tot} ratios, high Fe/Mg values (Fig. 7) and
694 enrichment in Fe_2O_{3T}. Abyssal peridotites usually contain between 8 and 9 wt.% FeO_T (Bodinier
695 and Godard, 2003) that would lead to a maximum Fe_2O_{3T} content between ~9 and 10 wt.% after
696 total oxidation of FeO to Fe_2O_3. At the smooth seafloor areas, the IOH-free serpentinites
697 containing between 7 and 10 wt.% (Fig. 9), the high Fe_2O_{3T} content in most of the IOH-
698 serpentinites can be explained by late oxidation of magnetite and serpentine. However,
699 exception occurs for samples SMS 4-2-1 and 11-2-11 (and to some extent SMS 5-4-17), as their
700 Fe_2O_{3T} content is significantly higher than the value that can be reached by total oxidation
701 suggesting that other interaction with previous Fe-rich fluids occurred and led to such
702 enrichment (see Section 5.2.1). The IOH-serpentinites are characterized by high Na_2O content
703 that can be explained, similarly to other SMS serpentinites, by interaction with NaCl-rich
704 seawater. Nevertheless, their higher enrichment may be related either to longer period of
705 interaction with seawater or seawater-derived fluids as some IOH-serpentinites are located at a
706 remote distance from the ridge (e.g. SMS 11-2-11) or by highly NaCl-enriched fluids (such as
707 hydrothermal brines). Additional halite salts would then precipitate and be mixed with IOH
708 assemblage.
709 The precipitation of IOH during this late oxidative alteration event leads to high
710 concentrations in La and Pr (Fig. 10 and 12), the La/Ce ratios being up to 20 and 7.9 for IOH-

serpentinites respectively northward and southward, and flat REE patterns (Fig. 12). Indeed, iron oxides and hydroxides are known to scavenge REE from fluids (Bau, 1999; Bau and Koschinsky, 2009). REE spectrum of IOH separated from SMS 11-2-11 (Fig. 12), whose concentrations are between 1 and 10 x PM, reflect this scavenging process. In addition, the La and Pr enrichments are responsible for the most negative Ce anomalies on the REE spectra of the SMS serpentinites (Fig. 10 and 12). Similarly as REE, the high FME concentrations (As, Cd, Sb; Fig. 11) of the IOH-serpentinites can be related to the occurrences of iron (hydro)oxides. Indeed, several studies reported that these element can be adsorbed on metals (Caillaud et al., 2009; Giménez et al., 2007). It is worthwhile to note that occurrences of IOH in the serpentinites do not lead to higher concentration in Li and B (Fig. 11), strengthening that their incorporation in serpentinites is not linked to the formation of oxides, but rather to the precipitation of serpentine. In conclusion, post-serpentinization processes and long-time fluid-rock interaction under oxidizing conditions favor the incorporation of trace elements into serpentinites implying thus that the oceanic lithosphere constitutes a sink for these elements.

Alteration of serpentine under low-temperature and oxidizing conditions usually leads to the formation of clays (Caillaud et al., 2006; Destrigneville et al., 1998; Karpoff et al., 2017; Venturelli et al., 1997). However, no clay could be identified in the IOH-serpentinites (see Results part and Appendix A) that could be related to the very low initial Al content of the SMS serpentinites.

6. Conclusions

Effects of serpentinization on element mass transfer between peridotites and seawater, seawater-derived and hydrothermal fluids were investigated for serpentinites collected on the smooth seafloor areas of the SWIR, and especially on the western corridor. These serpentinites

clearly show an increase in LOI, visual serpentinisation degree and oxidation degree (Fe^{3+}/Fe_{tot}) with distance from the ridge, allowing thus to establish distance profiles of serpentinization for both major and trace elements and to shed light on the consequences of fluid-rock interactions during long-lived exhumation and hydration history in an ultra-slow spreading context.

Significant changes in major and trace elements concentrations of the SMS serpentinites can be related to magmatic or secondary fluid-rock interaction processes. Indeed, melt-rock interaction affecting the peridotites led to enrichments in TiO_2, Fe_2O_{3T}, Na_2O and in some trace elements. High concentration in these elements are mainly observed in one serpentinite sample, suggesting that melt-rock interaction and refertilization processes are limited due to the very low magmatic activity. This low magmatic activity is also responsible for the near absence of magmatic plagioclase-rich lithologies (basalts and gabbros) at the SWIR axis and along the smoothseafloor areas, leading to the formation of fluids that differ significantly from those associated to black smoker-type systems. It is likely that these fluids are seawater-dominated, with a high Ce anomaly and the lack of Eu anomaly, a major difference with Eu-rich fluids from slow and fast-spreading ridges (e.g. MAR).

Nevertheless, three SMS serpentinites located furthest away from the ridge (e.g., SMS 11-2-11) present significant enrichments in Fe_2O_{3T}, Na_2O, metals, FME and LREE, suggesting interaction with high-temperature fluids, most likely during the first stages of exhumation via detachment faulting. These serpentinites, however, do not show sulfide mineralization commonly associated with circulation of black smoker-type hydrothermal fluids. This absence of sulfides may be explained either by late oxidative alteration or by circulation of a S-poor brine, both processes resulting in the formation of Fe-(hydro-)oxides. These hypotheses require further investigations on the S and Cl contents of the SMS serpentinites.

Long-term serpentinization at low-temperature does not influence Al_2O_3, its concentration being inherited from the protolith, and CaO, while its concentration can be higher in some SMS

761 serpentinites due to the precipitation of carbonate veins. Mobility of other major elements
762 (MgO, SiO_2, FeO, Na_2O) is also limited, their concentrations being nearly similar to that
763 expected from mantle partial melting. Serpentinization may be responsible for slight
764 compositional variations in MgO, FeO and SiO_2, but without a clear and systematic tendency.
765 Enrichments in Na_2O may likely be due to incorporation of salts from seawater-derived fluids
766 or hydrothermal brines circulating into the oceanic lithosphere. Trace elements, such as Li, B,
767 La, Pr, As, Sb, Cd show enrichments with distance from the ridge. Li and B enrichments are
768 likely related to serpentinization degree, implying that their concentrations might be used as
769 serpentinization proxies (in some specific cases).

770 The presence of (Fe-(hydro-)oxides), hematite and goethite, in highly serpentinized
771 peridotites indicate long-lived fluid-rock interaction with oxidizing conditions. For most of the
772 IOH-serpentinites, the apparent enrichment in Fe_2O_{3T} is the result of the total oxidation of iron
773 content during serpentinite and magnetite alteration. The lack of clays in these IOH-
774 serpentinites indicates that serpentine mineral is still stable for these conditions. Further O
775 isotope thermometry on these serpentinites is necessary to evaluate their temperature of
776 serpentinization. The late oxidative alteration that affected the IOH-serpentinites led to high
777 concentration in some trace elements, such as La, Pr, As, Sb and Cd.

778 We conclude that chemical exchanges during serpentinization at ultraslow-spreading ridges
779 happened during long-term interaction of the mature exhumed mantle with low-temperature
780 fluids. Amount of mass transfer is a function of ridge distance and hence of interaction time. In
781 addition, despite very low magmatic activity, high-temperature hydrothermal fluids may be
782 produced and interact with peridotites during early stages of detachment faulting. By exploring
783 the chemical compositions of serpentinites several kilometers away from the ridge axis, we
784 observe that fluid-rock interaction in oceanic context is only not limited to serpentinization

785 processes and that oxidizing alteration may greatly influence the oceanic lithosphere
786 composition.
787
788

Acknowledgments

Funding for petrographic and chemical analyses were provided by Labex Clervolc awarded to A.D. We thank J.-L. Devidal and J.-L. Piro from LMV Clermont-Ferrand for their respective help during electronic microprobe analyses and ICP-AES analyses. We are also grateful to M. Thibaut, C. Aineto and L. Menjot from Géosciences Environnement Toulouse for their assistance in the DRX analyses. G. Montagnac from the Laboratoire de Géologie de Lyon and ENS Lyon is also thanked for his assistance during RAMAN analyses.

798 **Figures, Tables and Appendices Captions**

799

800 Figure 1: Bathymetric map of the South West Indian Ridge (SWIR) between 62° and 65°E,
801 showing the location of the two West and East corridors where smooth seafloor were identified.
802 Location of dredges of the SMOOTHSEAFLOOR (SMS) expedition in these two corridors.
803 Inset shows the location of the smooth seafloor area along the SWIR, between the Melville
804 Fracture Zone and the Rodrigues Triple Junction (RTJ). Slightly modified from Sauter et al.
805 (2013). SEIR: South East Indian Ridge, CIR: Central Indian Ridge, RTJ: Rodrigues Triple
806 Junction.

807

808 Figure 2: Photographs and microphotographs of the SWIR SMS serpentinites. A and B:
809 Moderately serpentinized lherzolite (~50%, SMS 8-2-25), showing numerous relics of olivine
810 (ol), orthopyroxene (opx) and clinopyroxene (cpx) under crossed nicols (B) and in hand
811 specimen (A). C and D: Highly serpentinized harzburgite (~99%, SMS 2-2-11), showing bastite
812 (bast) and mesh serpentine (serp) crosscut by magnetite (mt) veins, in hand specimen (C) and
813 under natural light (D). E and F: Serpentinized and oxidized olivine websterite (SMS 5-4-17),
814 displaying amorphous iron oxides and hydroxides (IOH: hematite + goethite) at the former
815 emplacements of olivine, and a mixture of antigorite (ant), tremolite (tr) and chlorite (chl)
816 replacing the pyroxenes, in hand specimen (E) and under crossed nicols (F).

817

818 Figure 3: Microphotographs of secondary minerals in the SMS serpentinites. (A) Former
819 plagioclase altered to hydrogarnet (hydrogt) and chlorite (chl) in one metasomatized sample
820 (SMS 1-2-35, parallel nicols). (B) Cusps boundaries (indicated by arrows) between ortho- and
821 clinopyroxene in a metasomatized sample (SMS 1-2-35, crossed nicols). (C) Crystallized
822 goethite (goeth) associated with red-orange colored iron oxides and hydroxides (IOH, SMS 14-

5-8, reflected light). (D) Amorphous IOH in a strongly oxidized sample (SMS 4-2-11, reflected light). IOH are localized in the center of previous serpentine (serp) mesh cells, the magnetite network having disappeared.

Figure 4: Bulk rock MgO/SiO_2 and Al_2O_3/SiO_2 ratios of the SMS serpentinites, compared to MAR serpentinites (Paulick et al., 2006; Jöns et al., 2010; Kodolányi et al., 2012; Boschi et al., 2013) and SWIR serpentinites (Niu, 2004; Rouméjon, 2014; Rouméjon and Cannat, 2014). Terrestrial array and BSE value are from Jagoutz et al. (1979) and Hart and Zindler (1986).

Figure 5: Evolution of iron oxidation degree (Fe^{3+}/Fe_{Total}) with A) loss on ignition (LOI) and B) visual serpentinization degree of the SWIR SMS serpentinites.

Figure 6: Trace elements spidergrams of the SMS serpentinites compared to serpentinites from the SWIR (Niu, 2004; Rouméjon, 2014; Rouméjon and Cannat, 2014) and the MAR (Paulick et al., 2006; Delacour et al., 2008; Jöns et al., 2010; Kodolányi et al., 2012; Boschi et al., 2013). Values are normalized to primitive mantle and chondrites values of Sun and McDonough (1989).

Figure 7: Binary diagrams showing the evolution of major elements of the SMS serpentinites against TiO_2 concentrations, used as proxy of partial melting degree. Sample SMS 22-6-13 (melt-refertilized peridotite) is not considered in the description of correlation trends (see text). CaO trend excludes the two samples, SMS 10-5-6 and 29-5-41, containing calcite veins, and Fe/Mg trend excludes all IOH serpentinites. Error bars are comprised in the size of the marking point. SWIR and MAR references are the same as previous figures.

Figure 8 : Evolution of iron oxidation degree in the SMS serpentinites (west 62°30'E and east 64°40'E) as a function of ridge distance. Ridge axis is symbolized by the red line, and location of detachment faults is indicated by vertical dashed lines (approximated position on the seafloor taken from Sauter et al., 2013).

Figure 9 : Evolution of major elements with distance from the ridge for the serpentinites of the west smooth seafloor corridor of the SWIR. Error bars are comprised in the size of the marking points.

Figure 10 : Evolution of LREE (La, Ce and Pr) for the serpentinites of the west smooth seafloor corridor of the SWIR. Ce anomaly ($Ce/Ce^*=Ce_N/(La_N+Pr_N)^{0.5}$) is stable with the distance from the ridge serpentinization, while La and Pr contents increase.

Figure 11 : Evolution of FME for the serpentinites of the west smooth seafloor corridor of the SWIR. Li and B concentrations increase with distance and then with serpentinization degree, regardless of oxidation state. U is only enriched in samples that are strongly oxidized or contain high content of carbonates. Sb, As and Cd contents increase with oxidation degree of the rock.

Figure 12: REE spectra of the serpentinites of the west smooth seafloor corridor of the SWIR, compared to the MAR (Paulick et al., 2006; Delacour et al., 2008; Jöns et al., 2010; Kodolányi et al., 2012; Boschi et al., 2013) and SWIR serpentinites (Niu, 2004; Rouméjon, 2014; Rouméjon and Cannat, 2014). The SMS west corridor serpentinites are characterized by an overall depletion in REE, a negative Ce anomaly and an absence of Eu positive anomaly. The highest LREE concentrations (apart from Ce) corresponds to the IOH-bearing samples. Table

873 1: Sample names, locations from the ridge, protolith, primary and secondary mineralogical
874 assemblages, texture, serpentinization degree, and melt-rock interaction evidences of the
875 smooth seafloor serpentinites. Serpentinization degree was calculated as the sum of all
876 secondary phases modal proportions.
877
878 Table 2: Bulk major and trace elements compositions of the smooth seafloor serpentinites.
879
880 Appendix A: 1) X-Rays Diffraction (XRD) spectra on oriented section showing the diffraction
881 peaks of serpentine lizardite 1T, talc and clinochlore. 2) RAMAN spectrum of a lizardite +
882 antigorite mixture in a bastite of SMS 1-2-35.
883
884 Appendix B: Electron Microprobe compositions of primary and secondary minerals from the
885 SWIR SMS serpentinites
886

887 **References:**

888

889 Alt, J.C., 2004. Alteration of the upper oceanic: mineralogy, chemistry and processes. In:
890 Davies, E. E., Eldferfield, H. (Ed) Hydrogeology of the Oceanic Lithosphere, 495-533.
891 Cambridge Univ. Press, United-Kingdom.

892 Alt, J.C., Schwarzenbach, E.M., Früh-Green, G.L., Shanks, W.C., Bernasconi, S.M., Garrido,
893 C.J., Crispini, L., Gaggero, L., Padrón-Navarta, J.A., Marchesi, C., 2013. The role of
894 serpentinites in cycling of carbon and sulfur: Seafloor serpentinization and subduction
895 metamorphism. Lithos 178, 40–54. https://doi.org/10.1016/j.lithos.2012.12.006

896 Andreani, M., Escartin, J., Delacour, A., Ildefonse, B., Godard, M., Dyment, J., Fallick, A.E.,
897 Fouquet, Y., 2014. Tectonic structure, lithology, and hydrothermal signature of the
898 Rainbow massif (Mid-Atlantic Ridge 36°14'N). Geochemistry, Geophysics, Geosystems
899 15. https://doi.org/10.1002/2014GC005269.Received

900 Andreani, M., Muñoz, M., Marcaillou, C., Delacour, A., 2013. µXANES study of iron redox
901 state in serpentine during oceanic serpentinization. Lithos 178, 70–83.
902 https://doi.org/10.1016/j.lithos.2013.04.008

903 Barton, M.D., Johnson, D.A., 2000. Alternative brine sources for Fe-oxide(-Cu-Au) systems:
904 implications for hydrothermal alteration and metals. Hydrothermal Iron Oxide Copper-
905 Gold & Related Deposits: A Global Perspective 43–60.

906 Bau, M., 1999. Scavenging of dissolved yttrium and rare earths by precipitating iron
907 oxyhydroxide: experimental evidence for Ce oxidation, Y-Ho fractionation, and
908 lanthanide tetrad effect. Geochimica et Cosmochimica Acta 63, 67–77.

909 Bau, M., Koschinsky, A., 2009. Oxidative scavenging of cerium on hydrous Fe oxide :
910 Evidence from the distribution of rare earth elements and yttrium between Fe oxides and
911 Mn oxides in hydrogenetic ferromanganese crusts. Geochemical Journal 43, 37–47.

912 Bodinier, J., Godard, M., 2003. Orogenic, Ophiolitic and Abyssal Peridotites. Treatise on
913 Geochemistry. In: Carlson R.W. (Ed) Mantle and Core. Treatise on Geochemistry vol. 2.
914 Elsevier Science Ltd., pp. 103-170.
915 Borghini, G., Rampone, E., 2007. Postcumulus processes in oceanic-type olivine-rich
916 cumulates: The role of trapped melt crystallization versus melt/rock interaction.
917 Contributions to Mineralogy and Petrology 154, 619–633.
918 https://doi.org/10.1007/s00410-007-0217-5
919 Boschi, C., Dini, A., Früh-Green, G.L., Kelley, D.S., 2008. Isotopic and element exchange
920 during serpentinization and metasomatism at the Atlantis Massif (MAR 30°N): Insights
921 from B and Sr isotope data. Geochimica et Cosmochimica Acta 72, 1801–1823.
922 https://doi.org/10.1016/j.gca.2008.01.013
923 Caillaud, J., Proust, D., Philippe, S., Fontaine, C., Fialin, M., 2009. Trace metals distribution
924 from a serpentinite weathering at the scales of the weathering profile and its related
925 weathering microsystems and clay minerals. Geoderma 149, 199–208.
926 https://doi.org/10.1016/j.geoderma.2008.11.031
927 Caillaud, J., Proust, D., Righi, D., 2006. Weathering sequences of rock-forming minerals in a
928 serpentinite: Influence of microsystems on clay mineralogy. Clays and Clay Minerals 54,
929 87–100. https://doi.org/10.1346/CCMN.2006.0540111
930 Cannat, M., Bideau, D., Bougault, H., 1992. Serpentinized Peridotites and Gabbros In the Mid-
931 atlantic Ridge Axial Valley At 15 \textdegree\ 37’ N and 16 \textdegree\ 52’ N. Earth and
932 Planetary Science Letters 109, 87–106. https://doi.org/10.1016/0012-821X(92)90076-8
933 Cannat, M., Rommevaux-Jestin, C., Sauter, D., Deplus, C., Mendel, V., 1999. Formation of the
934 axial relief at the very slow spreading Southwest Indian Ridge (49° to 69°E). Journal of
935 Geophysical Research 104843, 822–825. https://doi.org/10.1029/1999JB900195

936 Cannat, M., Sauter, D., Mendel, V., Ruellan, E., Okino, K., Escartin, J., Combier, V., Baala,
937 M., 2006. Modes of seafloor generation at a melt-poor ultraslow-spreading ridge.
938 Geology 34, 605–608. https://doi.org/10.1130/G22486.1
939 Carignan, J., Hild, P., Mevelle, G., Morel, J., Yeghicheyan, D., 2001. Routine Analyses of
940 Trace Elements in Geological Samples using Flow Injection and Low Pressure On-Line
941 Liquid Chromatography Coupled to ICP-MS : A Study of Geochemical Reference
942 Materials, BR, DR-N, UB-N, AN-G and GH. Geostandards Newsletter 25, 187–198.
943 Chamberlain, J., 1965. Heazlewoodite and Awaruite in Serpentinites of the Eastern Townships,
944 Quebec. The Canadian Mineralogist 53, 519–522.
945 https://doi.org/10.1017/CBO9781107415324.004
946 Coleman, R.G., Keith, T.E., 1971. A Chemical Study of Serpentinization — Burro Moutain,
947 California. Journal of Petrology 12, 311–328. https://doi.org/10.1093/petrology/12.2.311
948 Debayle, E., Lévêque, J.J., 1997. Upper mantle heterogeneities in the Indian Ocean from
949 waveform inversion. Geophysical Research Letters 24, 245–248.
950 https://doi.org/10.1029/96GL03954
951 Decitre, S., Deloule, E., Reisberg, L., James, R., Agrinier, P., Mével, C., 2002. Behavior of Li
952 and its isotopes during serpentinization of oceanic peridotites. Geochemistry Geophysics
953 Geosystems 3, 1–20. https://doi.org/10.1029/2001GC000178
954 Delacour, A., Früh-Green, G.L., Bernasconi, S.M., Schaeffer, P., Kelley, D.S., 2008a. Carbon
955 geochemistry of serpentinites in the Lost City Hydrothermal System (30°N, MAR).
956 Geochimica et Cosmochimica Acta 72, 3681–3702.
957 https://doi.org/10.1016/j.gca.2008.04.039
958 Delacour, A., Früh-Green, G.L., Bernasconi, S.M., 2008b. Sulfur mineralogy and geochemistry
959 of serpentinites and gabbros of the Atlantis Massif (IODP Site U1309). Geochimica et
960 Cosmochimica Acta 72, 5111–5127. https://doi.org/10.1016/j.gca.2008.07.018

961 Deschamps, F., Godard, M., Guillot, S., Chauvel, C., Andreani, M., Hattori, K., Wunder, B.,
962 France, L., 2012. Behavior of fluid-mobile elements in serpentines from abyssal to
963 subduction environments: Examples from Cuba and Dominican Republic. Chemical
964 Geology 312–313, 93–117. https://doi.org/10.1016/j.chemgeo.2012.04.009
965 Deschamps, F., Godard, M., Guillot, S., Hattori, K., 2013. Geochemistry of subduction zone
966 serpentinites: A review. Lithos 178, 96–127. https://doi.org/10.1016/j.lithos.2013.05.019
967 Deschamps, F., Guillot, S., Godard, M., Andreani, M., Hattori, K., 2011. Serpentinites act as
968 sponges for fluid-mobile elements in abyssal and subduction zone environments. Terra
969 Nova 23, 171–178. https://doi.org/10.1111/j.1365-3121.2011.00995.x
970 Destrigneville, C.M., Karpoff, A.M., Charpentier, D. 1998. Modelling the halmyrolytic
971 formation of palygorskite from serpentinite. In: Arehart and Hulston (Eds) Water-rock
972 interaction, pp. 715-715
973 Dick, H.J.B., Bullen, T., 1984. Chromian spinel as a petrogenetic indicator in abyssal and
974 alpine-type peridotites and spatially associated lavas. Contributions to Mineralogy and
975 Petrology 86, 54–76. https://doi.org/10.1007/BF00373711
976 Douville, E., Charlou, J.L., Oelkers, E.H., Bienvenu, P., Jove Colon, C.F., Donval, J.P.,
977 Fouquet, Y., Prieur, D., Appriou, P., 2002. The rainbow vent fluids (36°14'N, MAR):
978 The influence of ultramafic rocks and phase separation on trace metal content in Mid-
979 Atlantic Ridge hydrothermal fluids. Chemical Geology 184, 37–48.
980 https://doi.org/10.1016/S0009-2541(01)00351-5
981 Dupré, B., Allègre, C.J., 1983. Pb-Sr isotope variation in Indian Ocean basalts and mixing
982 phenomena. Nature, 303.
983 Evans, B.W., 2008. Control of the products of serpentinization by the Fe2+ Mg-1 exchange
984 potential of olivine and orthopyroxene. Journal of Petrology 49, 1873–1887.
985 https://doi.org/10.1093/petrology/egn050

986 Finlow-Bates, T., Stumpfl, E.F., 1981. The behaviour of so-called immobile elements in
987 hydrothermally altered rocks associated with volcanogenic submarine-exhalative ore
988 deposits. Mineralium Deposita 16, 319–328. https://doi.org/10.1007/BF00202743
989 Frisby, C., Bizimis, M., Mallick, S., 2016. Seawater-derived rare earth element addition to
990 abyssal peridotites during serpentinization. Lithos 248–251, 432–454.
991 https://doi.org/10.1016/j.lithos.2016.01.025
992 Frisby, C., Foustoukos, D.I., Bizimis, M., 2019. Rare earth element uptake during olivine/water
993 hydrothermal interaction. Lithos 332–333, 147–161.
994 Frost, B.R., 1985. On the stability of sulfides, oxides, and native metals in serpentinite. Journal
995 of Petrology 26, 31–63.
996 Gautheron, C., Moreira, M., Gerin, C., Tassan-Got, L., Bezos, A., Humler, E., 2015. Constraints
997 on the DUPAL anomaly from helium isotope systematics in the Southwest Indian mid-
998 ocean ridge basalts. Chemical Geology 417, 163–172.
999 https://doi.org/10.1016/j.chemgeo.2015.10.005
1000 Giménez, J., Martínez, M., de Pablo, J., Rovira, M., Duro, L., 2007. Arsenic sorption onto
1001 natural hematite, magnetite, and goethite. Journal of Hazardous Materials 141, 575–580.
1002 https://doi.org/10.1016/j.jhazmat.2006.07.020
1003 Hart, S.R., Zindler, A., 1986. In search of a bulk-Earth composition. Chemical Geology 57,
1004 247–267. https://doi.org/10.1016/0009-2541(86)90053-7
1005 Hattori, K., Guillot, S., 2003. Volcanic fronts form as a consequence of serpentinite dehydration
1006 in the forearc mantle wedge. Geology 31, 525–528.
1007 Ishikawa, T., Nakamura, E., 1992. Boron isotope geochemistry of the oceanic crust from
1008 DSDP/ODP Hole 504B. Geochimica et Cosmochimica Acta 56, 1633–1639.
1009 https://doi.org/10.1016/0016-7037(92)90230-G
1010 Jagoutz, E., Palme, H., Baddenhausen, H., Blum, K., Cendales, M., Dreibus, G., Spettel, B.,

Lorenz, V., Wänke, H., 1979. The abundances of major, minor and trace elements in the earth's mantle as derived from primitive ultramafic nodules. Geochimica et Cosmochimica Acta 11 (2), 2031–2050.

Jöns, N., Bach, W. Klein, F. 2010. Magmatic influence on reaction paths and element transport during serpentinization. Chemical Geology 274, 169-211.

Kanehira, K., Banno, S., Yiu, S., 1975. Awaruite , Heazlewoodite , and Native Copper in Serpentinized Peridotite From the Mineoka District , Southern Boso Peninsula. Petr Econ Geol 70, 388–394.

Karpoff, A.M., Lagabrielle, Y., Boillot, G., Giraudeau, J., 1989. L'authigenèse océanique de palygorskite par halmyrolyse de péridotites serpentinisées (Marge de Galice): ses implications géodynamiques. Comptes Rendus Académie des Sciences, 308-647-654.

Karpoff, A.M., Sauter, D., Cannat, M., Ulrich, M., Manatschal, G, 2017. Fe-SO ixides tracing on-going low-temperature hydorthermal alteration of exhumed serpentinites at ultra-slow spreaing South West Indian Ridge. Procedia Earth Planetary Science 17, 280-283.

Karthe, S., Szargan, R., Suoninen, E., 1993. Oxidation of pyrite surfaces: a photoelectron spectroscopic study. Applied Surface Science 72, 157–170. https://doi.org/10.1016/0169-4332(93)90007-X

Kelley, D.S., Karson, J. a, Blackman, D.K., Früh-Green, G.L., Butterfield, D. a, Lilley, M.D., Olson, E.J., Schrenk, M.O., Roe, K.K., Lebon, G.T., Rivizzigno, P., 2001. An off-axis hydrothermal vent field near the Mid-Atlantic Ridge at 30 degrees N. Nature 412, 145–9. https://doi.org/10.1038/35084000

Kimball, K.L., 1990. Effects of hydrothermal alteration on the compositions of chromian spinels. Contributions to Mineralogy and Petrology 105, 337–346. https://doi.org/10.1007/BF00306543

1035 Kodolányi, J., Pettke, T., 2011. Loss of trace elements from serpentinites during fluid-assisted
1036 transformation of chrysotile to antigorite - An example from Guatemala. Chemical
1037 Geology 284, 351–362. https://doi.org/10.1016/j.chemgeo.2011.03.016
1038 Kodolányi, J., Pettke, T., Spandler, C., Kamber, B.S., Ling, K.G., 2012. Geochemistry of ocean
1039 floor and fore-arc serpentinites: Constraints on the ultramafic input to subduction zones.
1040 Journal of Petrology 53, 235–270. https://doi.org/10.1093/petrology/egr058
1041 Komor, S.C., Grove, T.L., Hébert, R., 1990. Abyssal peridotites from ODP Hole 670A (21
1042 10'N, 45 02'W): residues of mantle melting exposed by non-constructive axial
1043 divergence. Proceedings of Ocean Drilling Program, Scientific Results 106, 85–101.
1044 https://doi.org/10.2973/odp.proc.sr.106109.128.1990
1045 Lee, C.T.A., Oka, M., Luffi, P., Agranier, A., 2008. Internal distribution of Li and B in
1046 serpentinites from the feather River Ophiolite, California, based on laser ablation
1047 inductively coupled plasma mass spectrometry. Geochemistry, Geophysics, Geosystems
1048 9, 1–14. https://doi.org/10.1029/2008GC002078
1049 Legrand, D.L., Bancroft, G.M., Nesbitt, H.W., 2005. Oxidation/alteration of pentlandite and
1050 pyrrhotite surfaces at pH 9.3: Part 1. Assignment of XPS spectra and chemical trends.
1051 American Mineralogist 90, 1042–1054. https://doi.org/10.2138/am.2005.1691
1052 Malvoisin, B., 2015. Mass transfer in the oceanic lithosphere: Serpentinization is not
1053 isochemical. Earth and Planetary Science Letters 430, 75–85.
1054 https://doi.org/10.1016/j.epsl.2015.07.043
1055 Maxwell, J.A., 1968. Rock and Mineral Analysis, Interscience, New-York, 324-326
1056 McCaig, A.M., Cliff, R.A., Escartin, J., Fallick, A.E., MacLeod, C.J., 2007. Oceanic
1057 detachment faults focus very large volumes of black smoker fl uids. Geology 35, 935–938.
1058 https://doi.org/10.1130/G23657A.1
1059 McCaig, A.M., Delacour, A., FAllick, A.., Castelain, T., 2010. Detachement fault control on

hydrothermal ciruclation systems: interpreting the subsurface beneath the TAG hydrothermal field using isotopic and geological evolution of oceanic core complexes in the Atlantic. In: ROna P., Devey C., Dyment J., Murton B. (Eds) Diversity of hydrothermal systems on slow-spreading oceanic ridges. Geophysical Monograph Series vol. 188, 207-239.

Mével, C., 2003. Serpentinization of abyssal peridotites at mid-ocean ridges. Comptes Rendus Geoscience 335, 825–852. https://doi.org/10.1016/j.crte.2003.08.006

Meyzen, C.M., Toplis, M.J., Humler, E., Ludden, J.N., Mével, C., 2003. A discontinuity in mantle composition beneath the southwest Indian ridge. Nature 421, 731–733. https://doi.org/10.1038/nature01424

Muller, M.R., Robinson, C.J., Minshull, T.A., White, R.S., Bickle, M.J., 1997. Thin crust beneath ocean drilling program borehole 735B at the Southwest Indian Ridge? Earth and Planetary Science Letters 148, 93–107. https://doi.org/Doi 10.1016/S0012-821x(97)00030-7

Niu, Y., 2004. Bulk-rock major and trace element compositions of abyssal peridotites: Implications for mantle melting, melt extraction and post-melting processes beneath Mid-Ocean ridges. Journal of Petrology 45, 2423–2458. https://doi.org/10.1093/petrology/egh068

Niu, Y., Langmuir, C.H., Kinzler, R.J., 1997. The origin of abyssal peridotites: a new perspective. Earth and Planetary Science Letters 152, 251–265. https://doi.org/10.1016/S0012-821X(97)00119-2

O'Hanley, D.S., 1996. Serpentinites - Records of tectonic and petrological history.Oxford University Press.

Palandri, J.L., Reed, M.H., 2004. Geochemical models of metasomatism in ultramafic systems: Serpentinization, rodingitization, and sea floor carbonate chimney precipitation.

Geochimica et Cosmochimica Acta 68, 1115–1133. https://doi.org/10.1016/j.gca.2003.08.006

Paquet, M., Cannat, M., Brunelli, D., Hamelin, C., Humler, E., 2016. Effect of melt-mantle interactions on MORB chemistry at the easternmost Southwest Indian Ridge (61°–67°E). Geochemistry Geophysics Geosystems 17, 2825–2834. https://doi.org/10.1002/2016GC006406

Patriat, P., Sauter, D., Munschy, M., Parson, L., 1997. A survey of the Southwest Indian Ridge axis between Atlantis II Fracture Zone and the Indian Ocean triple junction: Regional setting and large scale segmentation. Marine Geophysical Research 19, 457–480. https://doi.org/10.1023/A:1004312623534

Paulick, H., Bach, W., Godard, M., De Hoog, J.C.M., Suhr, G., Harvey, J., 2006. Geochemistry of abyssal peridotites (Mid-Atlantic Ridge, 15°20′N, ODP Leg 209): Implications for fluid/rock interaction in slow spreading environments. Chemical Geology 234, 179–210. https://doi.org/10.1016/j.chemgeo.2006.04.011

Piccardo, G.B., Zanetti, A., Müntener, O., 2007. Melt/peridotite interaction in the Southern Lanzo peridotite: Field, textural and geochemical evidence. Lithos 94, 181–209. https://doi.org/10.1016/j.lithos.2006.07.002

Quinby-Hunt, M.S., Turekian, K.K., 1983. Distribution of elements in sea water. The Oceanography Report 130–132.

Rampone, E., Piccardo, G.B., Vannucci, R., Bottazzi, P., 1997. Chemistry and origin of trapped melts in ophioiitic peridotites. Geochimica et Cosmochimica Acta 61, 4557–4569. https://doi.org/10.1016/s0016-7037(97)00260-3

Richardson, S., Vaughan, D.J., 1989. Surface alteration of pentlandite and spectroscopic evidence for secondary violarite formation. Mineralogical Magazine 53, 213–222.

1109 Rouméjon, S., 2014. Serpentinisation des péridotites exhumées aux dorsales lentes : approches
1110 microstructurale , minéralogique et géochimique
1111 Rouméjon, S., Cannat, M., 2014. Serpentinization of mantle derived peridotites at mid ocaean
1112 ridges: mesh texture in the context of tectonic exhumation. Geochemistry, Geophysics,
1113 Geosystems 15, 2354–2379. https://doi.org/10.1002/2013GC005148.Received
1114 Rouméjon, S., Cannat, M., Agrinier, P., Godard, M., Andreani, M., 2015. Serpentinization and
1115 fluid pathways in tectonically exhumed peridotites from the southwest Indian ridge (62-
1116 65°E). Journal of Petrology 56, 703–734. https://doi.org/10.1093/petrology/egv014
1117 Salters, V.J.M., Dick, H.J.B., 2002. Mineralogy of the mid-ocean-ridge basalt source from
1118 neodymium isotopic composition of abyssal peridotites. Nature 418, 68–72.
1119 https://doi.org/10.1038/nature00886.1.
1120 Sauter, D., Cannat, M., Meyzen, C., Bezos, A., Patriat, P., Humler, E., Debayle, E., 2009.
1121 Propagation of a melting anomaly along the ultraslow Southwest Indian Ridge between
1122 46°E and 52°20′E: Interaction with the Crozet hotspot? Geophysical Journal International
1123 179, 687–699. https://doi.org/10.1111/j.1365-246X.2009.04308.x
1124 Sauter, D., Cannat, M., Rouméjon, S., Andreani, M., Birot, D., Bronner, A., Brunelli, D., Carlut,
1125 J., Delacour, A., Guyader, V., MacLeod, C.J., Manatschal, G., Mendel, V., Ménez, B.,
1126 Pasini, V., Ruellan, E., Searle, R., 2013. Continuous exhumation of mantle-derived rocks
1127 at the Southwest Indian Ridge for 11 million years. Nature Geoscience 6, 314–320.
1128 https://doi.org/10.1038/ngeo1771
1129 Schwarzenbach, E.M., Lang, S.Q.., Frueh-Green, G.L., Lilley, M., Bernasconi, S.M., Méhay,
1130 S., 2013. Sources and cycling of carbon in continental, serpentinite-hosted alkaline springs
1131 in the Voltri Massif, Italy. Lithos 177, 226-244.

1132 Seyfried, W.E., Dibble, W.E., 1979. Seawater-peridotite interaction at 300°C and 500 bars:
1133 implications for the origin of oceanic serpentinites. Geochimica et Cosmochimica Acta
1134 44, 309–321. https://doi.org/10.1016/0016-7037(80)90139-8
1135 Seyfried, W.E., Janecky, D.R., Mottl, M.J., 1984. Alteration of the oceanic crust: Implications
1136 for geochemical cycles of lithium and boron. Geochimica et Cosmochimica Acta 48, 557–
1137 569.
1138 Seyler, M., Brunelli, D., Toplis, M.J., Mével, C., 2011. Multiscale chemical heterogeneities
1139 beneath the eastern Southwest Indian Ridge (52°E-68°E): Trace element compositions of
1140 along-axis dredged peridotites. Geochemistry, Geophysics, Geosystems 12.
1141 https://doi.org/10.1029/2011GC003585
1142 Seyler, M., Cannat, M., Mével, C., 2003. Evidence for major-element heterogeneity in the
1143 mantle source of abyssal peridotites from the Southwest Indian Ridge (52° to 68° E).
1144 Geochemistry, Geophysics, Geosystems 4. https://doi.org/10.1029/2002GC000305
1145 Sharp, Z.D., Barnes, J.D., 2004. Water-soluble chlorides in massive seafloor serpentinites: A
1146 source of chloride in subduction zones. Earth and Planetary Science Letters 226, 243–
1147 254. https://doi.org/10.1016/j.epsl.2004.06.016
1148 Shervais, J.W., Kolesar, P., Andreasen, K., 2005. A Field and Chemical Study of
1149 Serpentinization — Stonyford , California : Chemical Flux and Mass Balance.
1150 International Geology Review 47, 1–23.
1151 Sinha, A.K., Hewitt, D.A., Rimstidt, J.D., 1986. Fluid interaction and element mobility in the
1152 development of ultramylonites. Geology 14, 883–886. https://doi.org/10.1130/0091-
1153 7613(1986)14<883
1154 Snow, J.E., Dick, H.J.B., 1995. Pervasive magnesium loss by marine weathering of peridotite.
1155 Geochimica et Cosmochimica Acta 59, 4219–4235. https://doi.org/10.1016/0016-
1156 7037(95)00239-V

1157 Spivack, A.., Edmond, J.., 1987. Boron isotope exchange between seawater and the oceanic
1158 crust. Geochimica et Cosmochimica Acta 51, 1033–1043. https://doi.org/10.1016/0016-
1159 7037(87)90198-0
1160 Sun, S. -s., McDonough, W.F., 1989. Chemical and isotopic systematics of oceanic basalts:
1161 implications for mantle composition and processes. Geological Society, London, Special
1162 Publications 42, 313–345. https://doi.org/10.1144/GSL.SP.1989.042.01.19
1163 Tang, Y., Zhai, Q.G., Hu, P.Y., Wang, J., Xiao, X.C., Wang, H.T., Tang, S.H., Lei, M., 2018.
1164 Rodingite from the Beila ophiolite in the Bangong–Nujiang suture zone,northern Tibet:
1165 New insights into the formation ofophiolite-related rodingite. Lithos 316–317, 33–47.
1166 https://doi.org/10.1016/j.lithos.2018.07.006
1167 Toft, P.B., Arkani-Hamed, J., Haggerty, S.E., 1990. The effects of serpentinization on density
1168 and magnetic susceptibility: a petrophysical model. Physics of the Earth and Planetary
1169 Interiors 65, 137–157.
1170 Venturelli, G., Contini, S., Bonazzi, A., Mangia, A., 1997. Weathering of ultramafic rocks and
1171 element mobility at Mt. Prinzera, Northern Apennines, Italy. Mineralogical Magazine 61,
1172 765–778.
1173 Vils, F., Pelletier, L., Kalt, A., Müntener, O., Ludwig, T., 2008. The Lithium, Boron and
1174 Beryllium content of serpentinized peridotites from ODP Leg 209 (Sites 1272A and
1175 1274A): Implications for lithium and boron budgets of oceanic lithosphere. Geochimica
1176 et Cosmochimica Acta 72, 5475–5504. https://doi.org/10.1016/j.gca.2008.08.005
1177 Von Herzen, R.P., 2204. Geothermal evidence for continuing hydrothermal ciruclation in older
1178 (> 60 M.y.) ocean crust. In: Davies, E. E., Eldferfield, H. (Ed) Hydrogeology of the
1179 Oceanic Lithosphere, 495-533. Cambridge Univ. Press, United-Kingdom.

1180 Warren, J.M., Shimizu, N., 2010. Cryptic Variations in Abyssal Peridotite Compositions :
1181 Evidence for Shallow-level Melt Infiltration in the Oceanic Lithosphere. Journal of
1182 Petrology 51, 395–423. https://doi.org/10.1093/petrology/egp096
1183
1184

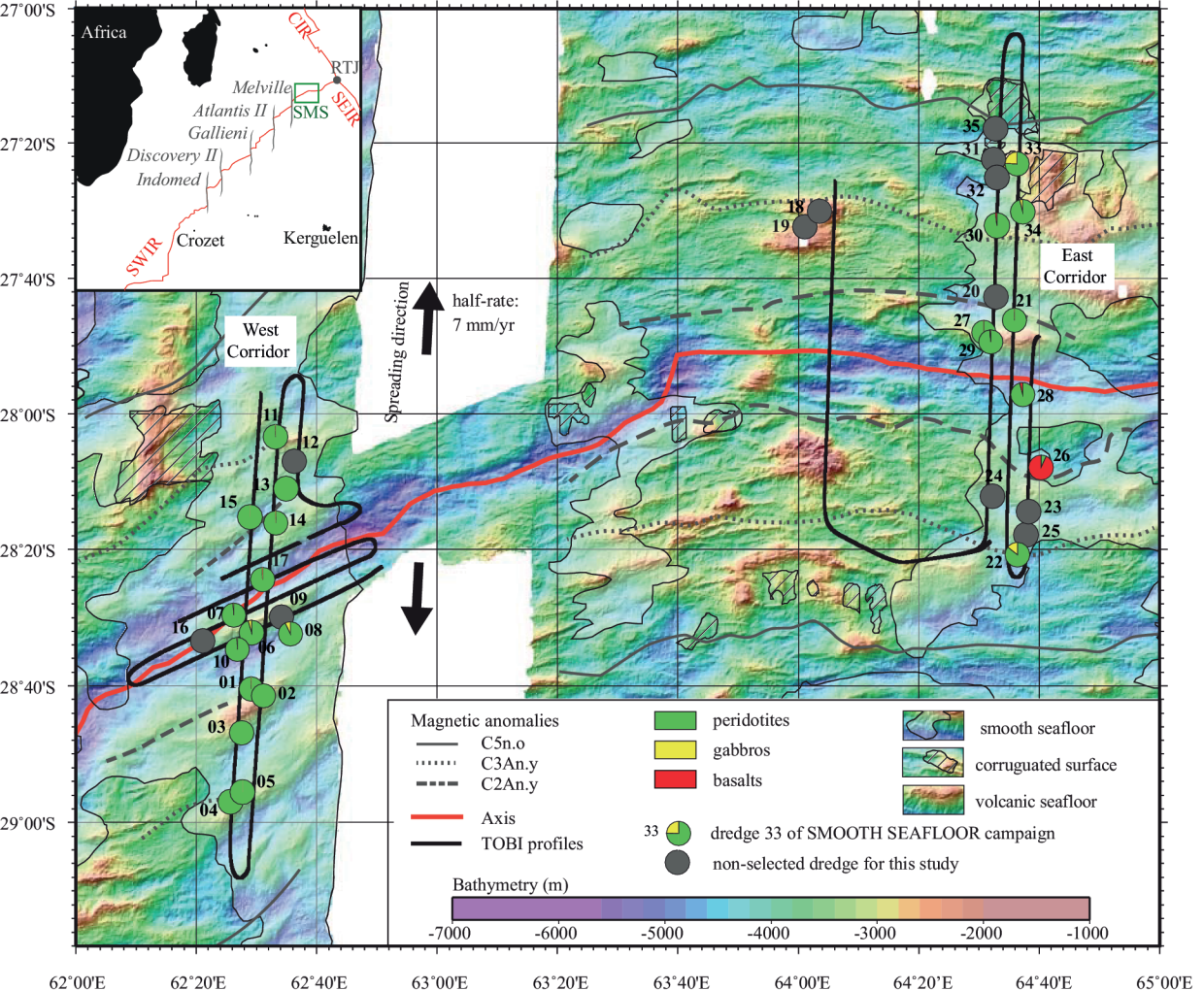
Africa
CIR
SEIR
RTJ
Melville
Atlantis II
Gallieni
Discovery II
Indomed
SMS
SWIR
Crozet
Kerguelen
West Corridor
East Corridor
Spreading direction
half-rate: 7 mm/yr
27°00'S
27°20'S
27°40'S
28°00'S
28°20'S
28°40'S
29°00'S
62°00'E
62°20'E
62°40'E
63°00'E
63°20'E
63°40'E
64°00'E
64°20'E
64°40'E
65°00'E
Magnetic anomalies
C5n.o
C3An.y
C2An.y
Axis
TOBI profiles
peridotites
gabbros
basalts
smooth seafloor
corruguated surface
volcanic seafloor
33 dredge 33 of SMOOTH SEAFLOOR campaign
non-selected dredge for this study
Bathymetry (m)
-7000
-6000
-5000
-4000
-3000
-2000
-1000

16 cm

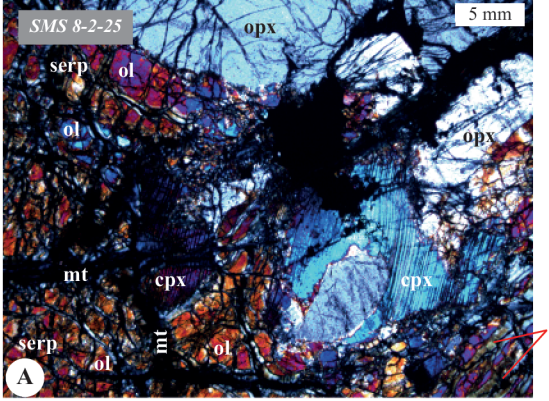
SMS 8-2-25
5 mm
opx
serp
ol
ol
opx
mt
cpx
cpx
serp
mt
ol
ol
A

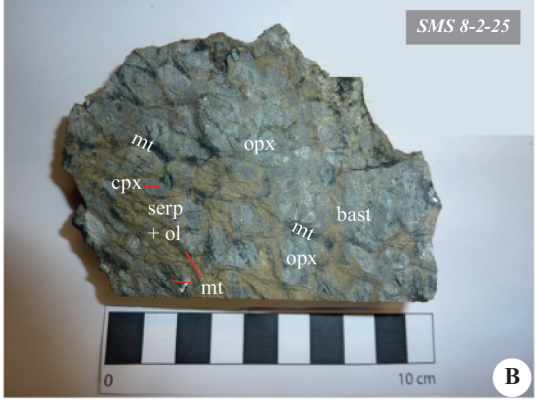
SMS 8-2-25
mt
opx
cpx
serp
+ ol
bast
mt
opx
mt
0
10 cm
B

serp


SMS 2-2-11
bast
serp + mt
bast
serp + mt
0
10 cm
C

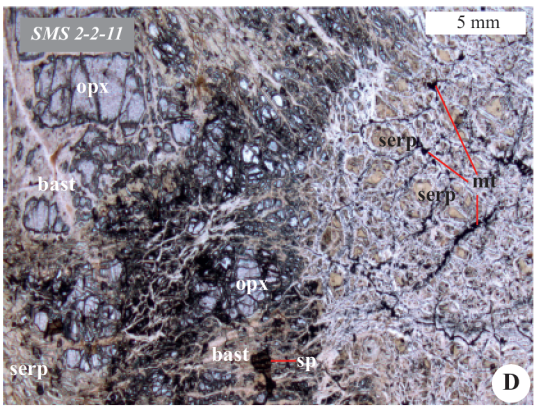
SMS 2-2-11
5 mm
opx
serp
bast
mt
serp
opx
serp
bast
sp
D

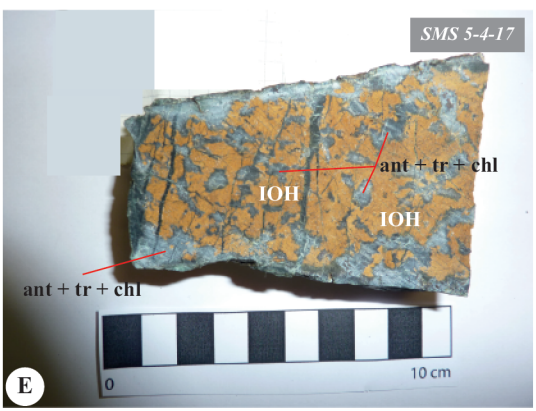
SMS 5-4-17
ant + tr + chl
IOH
IOH
ant + tr + chl
0
10 cm
E

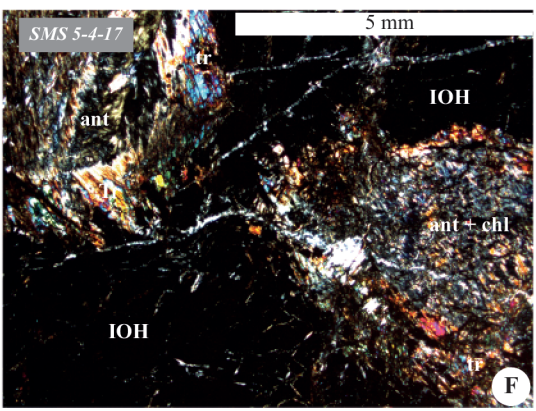
SMS 5-4-17
5 mm
tr
IOH
ant
ant + chl
IOH
tr
F

16 cm

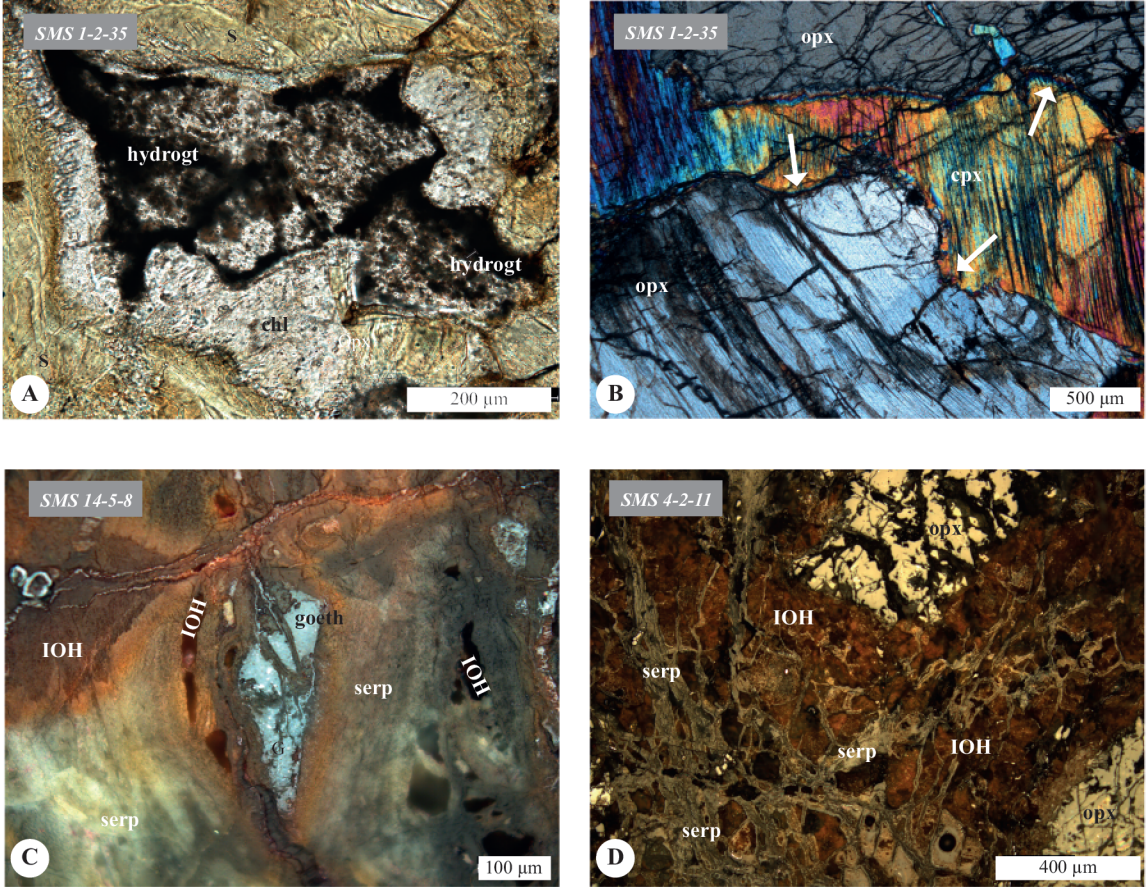
SMS 1-2-35
hydrogt
hydrogt
chl
cpx
A
200 µm
SMS 1-2-35
opx
cpx
opx
B
500 µm
SMS 14-5-8
IOH
IOH
goeth
serp
IOH
serp
C
100 µm
SMS 4-2-11
opx
IOH
serp
serp
IOH
serp
opx
D
400 µm

16 cm

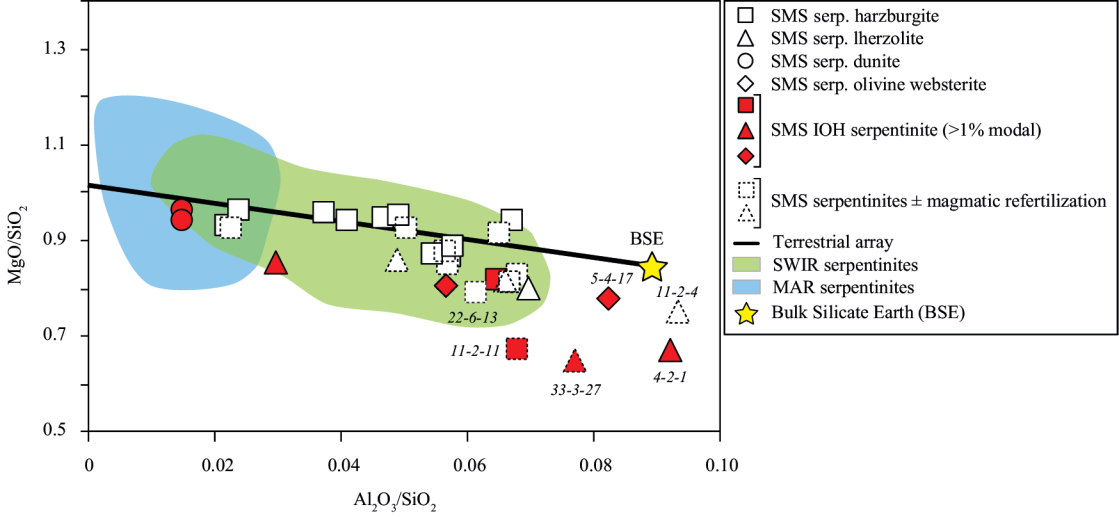
1.3
1.1
0.9
0.7
0.5
MgO/SiO2
0
0.02
0.04
0.06
0.08
0.10
Al2O3/SiO2
BSE
5-4-17
11-2-4
22-6-13
11-2-11
33-3-27
4-2-1
SMS serp. harzburgite
SMS serp. lherzolite
SMS serp. dunite
SMS serp. olivine websterite
SMS IOH serpentinite (>1% modal)
SMS serpentinites ± magmatic refertilization
Terrestrial array
SWIR serpentinites
MAR serpentinites
Bulk Silicate Earth (BSE)

16 cm

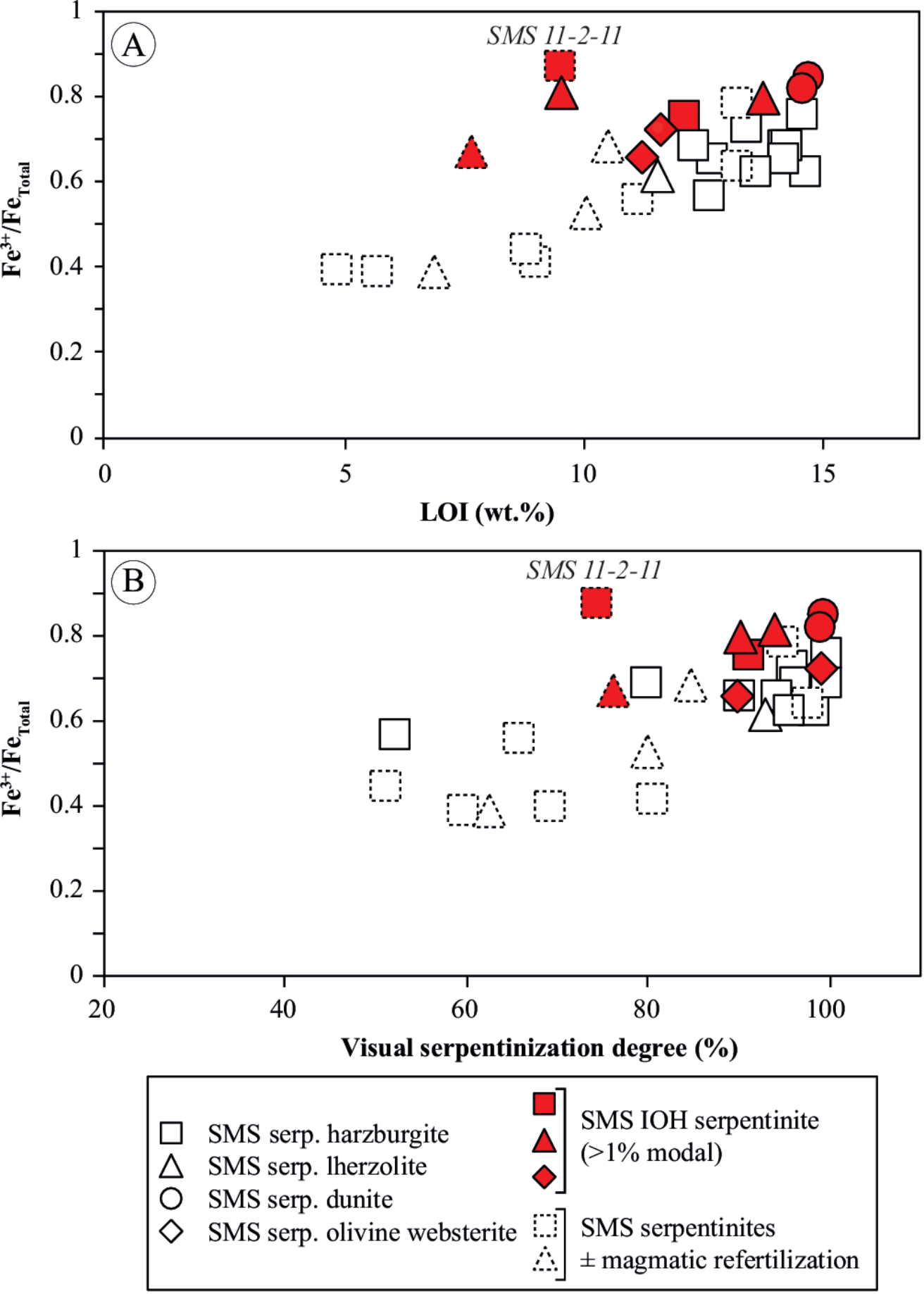
A
SMS 11-2-11
Fe3+/FeTotal
LOI (wt.%)
B
SMS 11-2-11
Fe3+/FeTotal
Visual serpentinization degree (%)
SMS serp. harzburgite
SMS serp. lherzolite
SMS serp. dunite
SMS serp. olivine websterite
SMS IOH serpentinite (>1% modal)
SMS serpentinites ± magmatic refertilization

9 cm

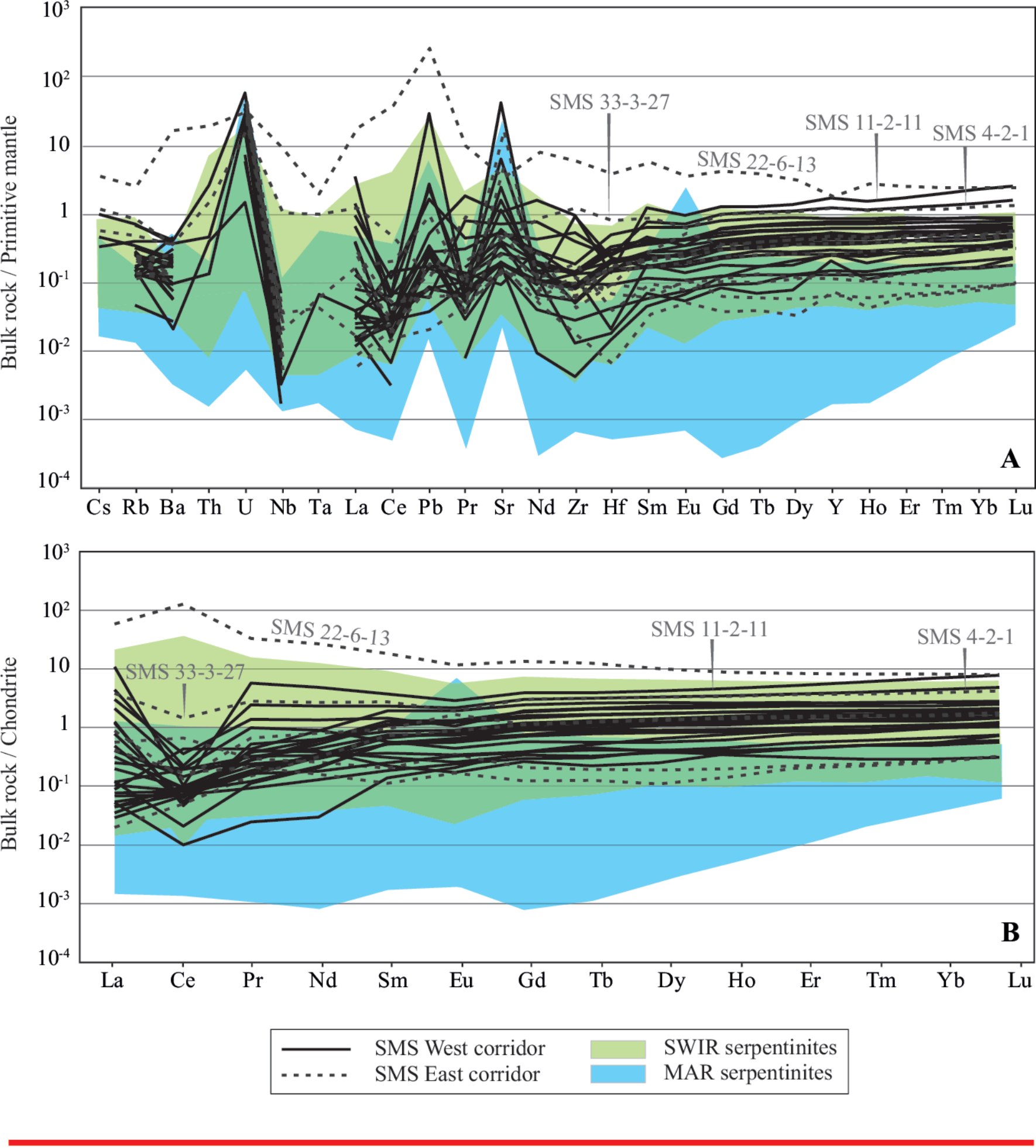
Bulk rock / Primitive mantle
SMS 33-3-27
SMS 11-2-11
SMS 4-2-1
SMS 22-6-13
A
Cs Rb Ba Th U Nb Ta La Ce Pb Pr Sr Nd Zr Hf Sm Eu Gd Tb Dy Y Ho Er Tm Yb Lu
Bulk rock / Chondrite
SMS 22-6-13
SMS 11-2-11
SMS 4-2-1
SMS 33-3-27
B
La Ce Pr Nd Sm Eu Gd Tb Dy Ho Er Tm Yb Lu
SMS West corridor
SMS East corridor
SWIR serpentinites
MAR serpentinites
12 cm

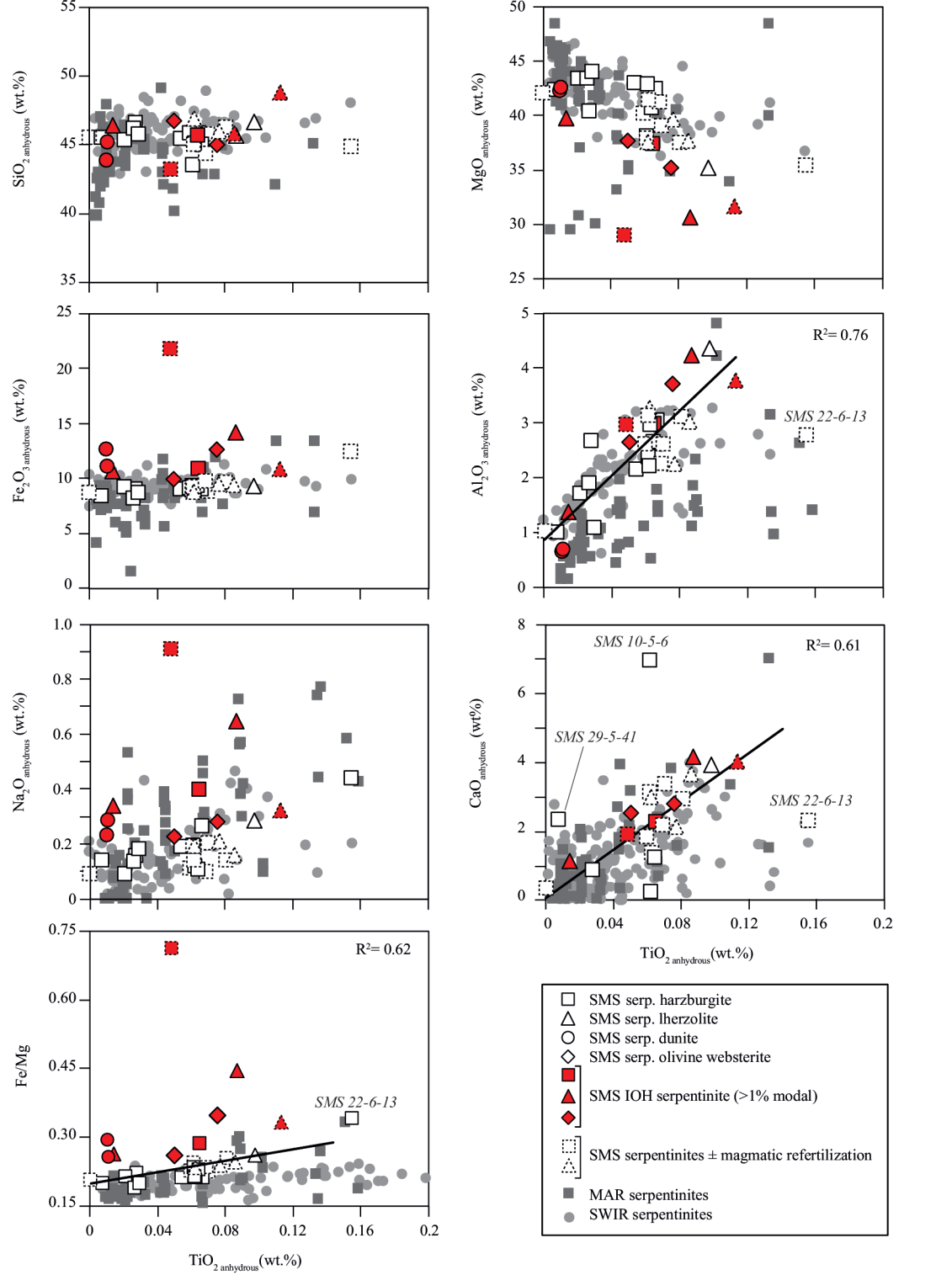
SiO2 anhydrous (wt.%)
MgO anhydrous (wt.%)
Fe2O3 anhydrous (wt.%)
Al2O3 anhydrous (wt.%)
R²= 0.76
SMS 22-6-13
Na2O anhydrous (wt.%)
CaO anhydrous (wt%)
SMS 10-5-6
R²= 0.61
SMS 29-5-41
SMS 22-6-13
Fe/Mg
R²= 0.62
SMS 22-6-13
TiO2 anhydrous (wt.%)
TiO2 anhydrous (wt.%)
SMS serp. harzburgite
SMS serp. lherzolite
SMS serp. dunite
SMS serp. olivine websterite
SMS IOH serpentinite (>1% modal)
SMS serpentinites ± magmatic refertilization
MAR serpentinites
SWIR serpentinites

15 cm

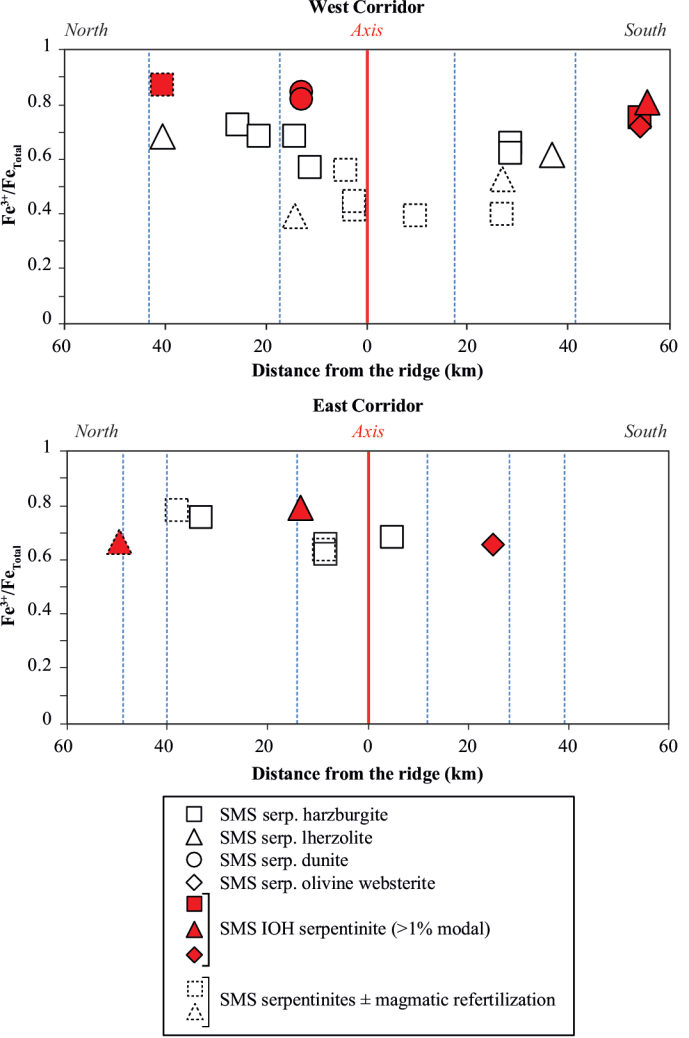
West Corridor
North
Axis
South
Fe3+/FeTotal
1
0.8
0.6
0.4
0.2
0
60
40
20
0
20
40
60
Distance from the ridge (km)
East Corridor
North
Axis
South
Fe3+/FeTotal
1
0.8
0.6
0.4
0.2
0
60
40
20
0
20
40
60
Distance from the ridge (km)
SMS serp. harzburgite
SMS serp. lherzolite
SMS serp. dunite
SMS serp. olivine websterite
SMS IOH serpentinite (>1% modal)
SMS serpentinites ± magmatic refertilization

9 cm

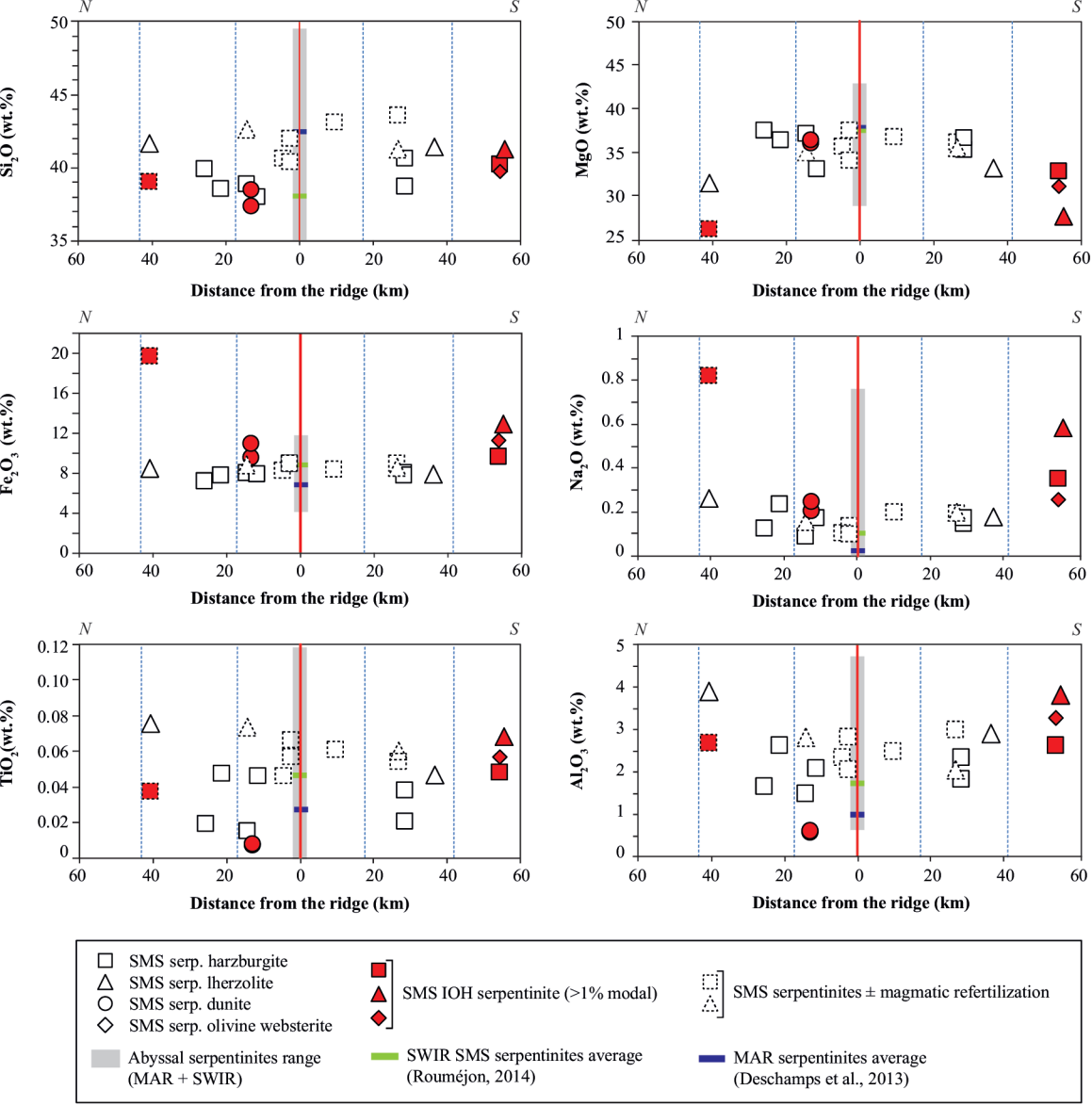
N
S
Si_2O (wt.%)
MgO (wt.%)
Fe_2O_3 (wt.%)
Na_2O (wt.%)
TiO_2(wt.%)
Al_2O_3 (wt.%)
Distance from the ridge (km)
SMS serp. harzburgite
SMS serp. lherzolite
SMS serp. dunite
SMS serp. olivine websterite
SMS IOH serpentinite (>1% modal)
SMS serpentinites ± magmatic refertilization
Abyssal serpentinites range (MAR + SWIR)
SWIR SMS serpentinites average (Rouméjon, 2014)
MAR serpentinites average (Deschamps et al., 2013)

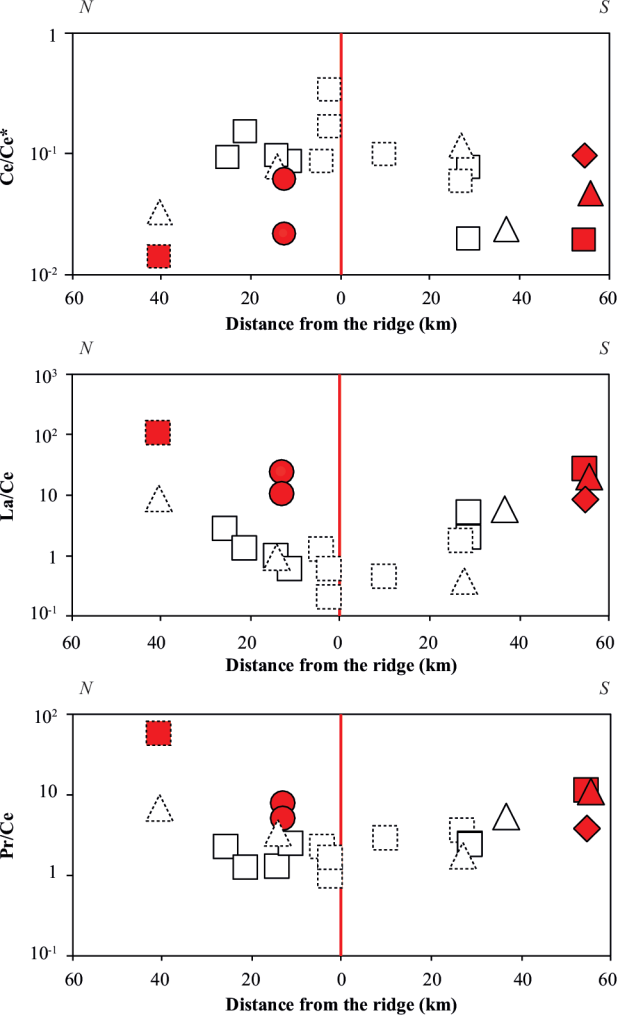
N
S
Ce/Ce*
1
10-1
10-2
60
40
20
0
20
40
60
Distance from the ridge (km)
N
S
La/Ce
10³
10²
10
1
10-1
60
40
20
0
20
40
60
Distance from the ridge (km)
N
S
Pr/Ce
10²
10
1
10-1
60
40
20
0
20
40
60
Distance from the ridge (km)
SMS serp. harzburgite
SMS serp. lherzolite
SMS serp. dunite
SMS serp. olivine websterite
SMS IOH serpentinite
(>1% modal)
SMS serpentinites
± magmatic refertilization

8 cm

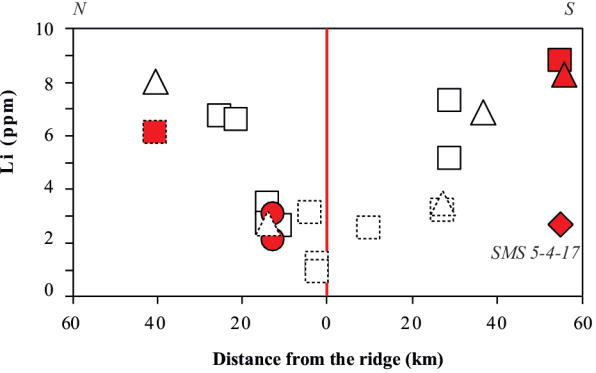
N
S
Li (ppm)
SMS 5-4-17
Distance from the ridge (km)

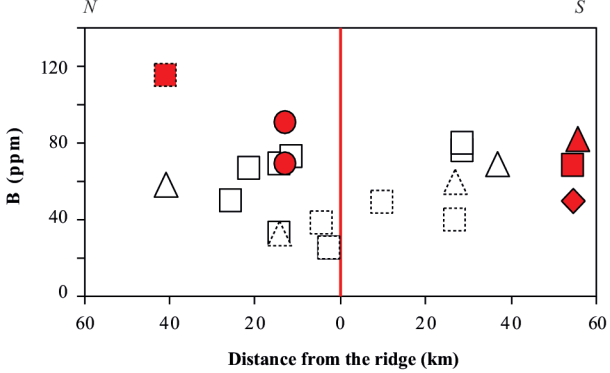
N
S
B (ppm)
Distance from the ridge (km)

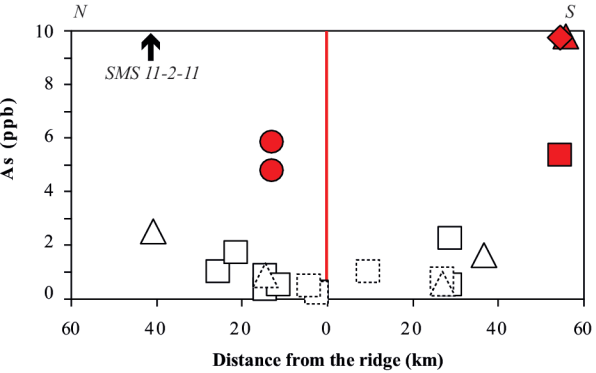
N
S
SMS 11-2-11
As (ppb)
Distance from the ridge (km)

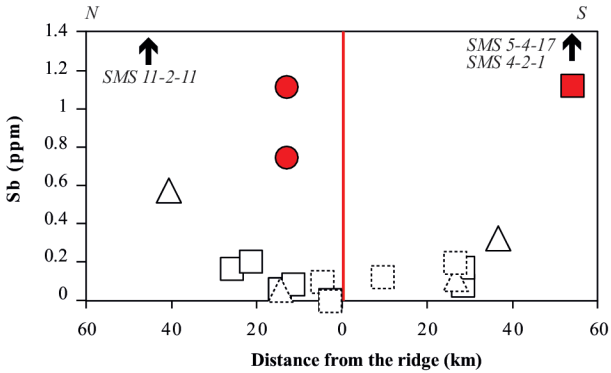
N
S
SMS 11-2-11
SMS 5-4-17
SMS 4-2-1
Sb (ppm)
Distance from the ridge (km)

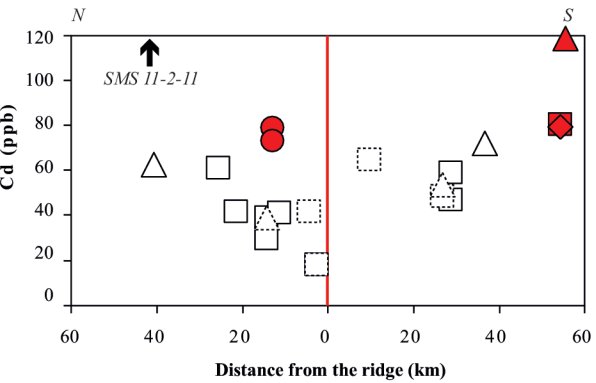
N
S
SMS 11-2-11
Cd (ppb)
Distance from the ridge (km)

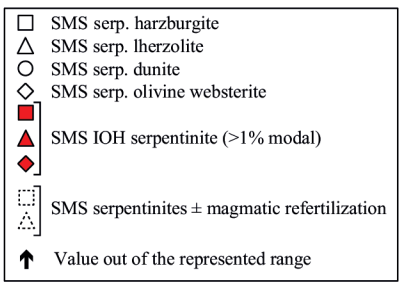
SMS serp. harzburgite
SMS serp. lherzolite
SMS serp. dunite
SMS serp. olivine websterite
SMS IOH serpentinite (>1% modal)
SMS serpentinites ± magmatic refertilization
Value out of the represented range

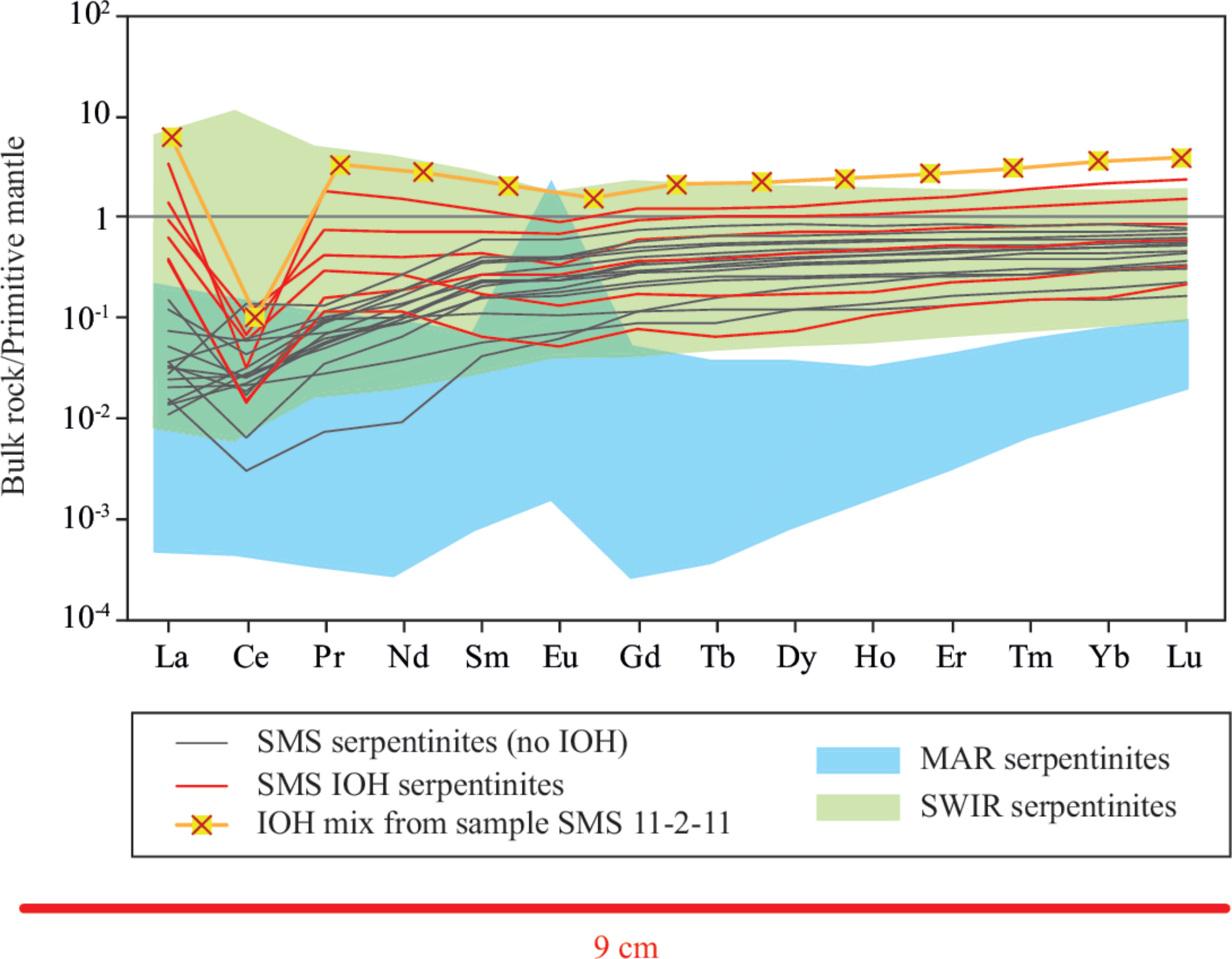
Bulk rock/Primitive mantle
10²
10
1
10⁻¹
10⁻²
10⁻³
10⁻⁴
La
Ce
Pr
Nd
Sm
Eu
Gd
Tb
Dy
Ho
Er
Tm
Yb
Lu
SMS serpentinites (no IOH)
SMS IOH serpentinites
IOH mix from sample SMS 11-2-11
MAR serpentinites
SWIR serpentinites
9 cm

Table 1: Sample names, locations from the ridge, protolith, primary and secondary mineralogical assemblages, texture, serpentinization degree, and melt-rock interaction evidences of the smooth seafloor serpentinites. Serpentinization degree was calculated as the sum of all secondary phases modal proportions.

Sample name (used in this study)	Ridge distance (km)	Protolith	Primary minerals (as relic)	Secondary minerals	Sulfides/oxides	Serpentine texture and veins	Serp. degree (%)	Melt-rock interaction evidences	Complementary analyses	Sample name from Smoothseafloor
SMS 1-2-1	26.7	harzburgite	ol + opx + cpx + sp	serp	mt ± pn	M	69	ol cryst		SMS_DR01_2_01
SMS 1-2-35	26.7	lherzolite	ol + opx + cpx + sp	serp + tr + chl + tlc + carb	mt ± pn	M + B ± Lv	74	plagio, cpx cryst	Raman	SMS_DR01_2_35
SMS 2-2-11	28.5	harzburgite	opx + cpx + sp	serp	mt ± mi ± cpy ± vt	M + B	90	–	Raman	SMS_DR02_2_11
SMS 2-2-17	28.5	harzburgite	sp	serp + tr + chl	± mt	M + B	98	–		SMS_DR02_2_17
SMS 3-2-1	36.4	lherzolite	opx + cpx + sp	serp + tr + chl ± tlc	± mt ± pn	M + B	93	–		SMS_DR03_2_01
SMS 4-2-1	55.2	lherzolite	opx + cpx + sp	serp + tr + tlc ± chl	hm + gt ± mt	M + B	94	–		SMS_DR04_2_01
SMS 5-4-14	53.9	harzburgite	opx + cpx + sp	serp ± tr ± chl ± tlc	mt + hm + gt ± pn ± aw	M + B + Cv	91	–		SMS_DR05_4_14
SMS 5-4-17	53.9	olivine websterite	cpx + sp	serp + tr + chl	hm + gt ± mt	M + Cv ± Lv	99	–		SMS_DR05_4_17
SMS 6-3-14	9.7	harzburgite	ol + opx + cpx + sp	serp	± mt ± hm ± gt ± pn	M ± Lv	60	ol cryst		SMS_DR06_3_14
SMS 7-3-7	4.2	harzburgite	ol + opx + cpx + sp	serp + tr + chl	± mt ± pn ± mi	M + B + Cv	66	plagio	Raman	SMS_DR07_3_37
SMS 8-2-17	14.2	harzburgite	± sp	serp + chl + tlc	± mt	M + B + Cv ± Lv	100	–		SMS_DR08_2_17
SMS 8-2-25	14.2	lherzolite	ol + opx + cpx + sp	serp + carb	mt ± pn	M + B	63	cpx cryst		SMS_DR08_2_25
SMS 10-5-6	11.2	harzburgite	ol + opx + cpx + sp	serp + tr + tlc + carb	± mt ± pn	M + B ± Lv	52	–		SMS_DR10_5_06
SMS 11-2-4	40.6	lherzolite	opx + cpx + sp	serp + tr + chl + tlc	± mt ± hm ± gt ± pn	M + B ± Lv	85	cpx cryst		SMS_DR11_2_04
SMS 11-2-11	40.6	harzburgite	ol + opx + cpx + sp	serp	hm + gt ± mt	M	74	ol cryst		SMS_DR11_2_11
SMS 13-4-11	25.5	harzburgite	opx + sp	serp + chl	± mt	M + B + Cv	96	–		SMS_DR13_4_11
SMS 14-5-1	12.7	dunite	sp	serp	hm + gt ± pn ± mt	M + Ct ± Lv	98	–	Raman	SMS_DR14_5_01
SMS 14-5-8	12.7	dunite	sp	serp	mt ± hm ± gt	M + Cv	99	–	Raman	SMS_DR14_5_08
SMS 15-3-16	21.2	harzburgite	opx + sp	serp	± mt	M + B + Cv	96	–		SMS_DR15_3_16
SMS 17-4-19	2.4	harzburgite	ol + opx + cpx + sp	serp	mt ± pn	M + B	81	ol cryst		SMS_DR17_4_19
SMS 17-4-32	2.4	harzburgite	ol + opx + cpx + sp	serp ± carb	mt ± pn	M + B	51	cpx cryst	Raman	SMS_DR17_4_32
SMS 21-5-6	16.4	lherzolite	opx + cpx + sp	serp + tr + chl	mt + hm + gt	M + B + Ct ± Lv	90	–		SMS_DR21_5_6
SMS 22-6-13	45.5	harzburgite	opx + cpx	serp ± chl	mt	M + B + Ct	89	plagio		SMS_DR22_6_13
SMS 26-2-11	24.2	olivine websterite	ol	serp + tr + chl	mt + hm + gt ± pn	V	90	–		SMS_DR26_2_11
SMS 27-2-19	11.2	harzburgite	opx + cpx + sp	serp + tr + tlc	± mt ± pn ± mi	M + B ± Lv	98	cpx cryst		SMS_DR27_2_19
SMS 28-4-10	3.9	harzburgite	opx + cpx + sp	serp + carb	mt ± pn ± mi ± cpt	M + B + Ct ± Lv	80	–		SMS_DR28_4_10
SMS 29-5-41	10.6	harzburgite	cpx + sp	serp + tr + tlc + carb ± chl	mt	M + B	94	–		SMS_DR29_5_41
SMS 29-6-13	10.6	harzburgite	opx + cpx + sp	serp ± chl	± mt ± hm ± gt ± pn	M + B + Cv	95	–		SMS_DR29_6_13
SMS 30-2-2	39.4	harzburgite	± sp	serp	± mt	M + B + Ct ± Lv	100	–		SMS_DR30_2_2
SMS 33-3-27	57.9	lherzolite	opx + cpx	serp	mt + hm + gt	M + B	76	cpx cryst		SMS_DR33_3_27
SMS 34-2-17	44.8	harzburgite	opx + cpx + sp	serp + chl ± tr ± tlc ± carb	mt	M + B + Cv	95	plagio, cpx cryst		SMS_DR34_2_17

Abbreviations: ± indicates that a phase modal proportion is strictly < 1%
Primary minerals: ol: olivine, opx: orthopyroxene, cpx: clinopyroxene, sp: spinel,
Serpentine texture: M: mesh, B: bastite (after pyroxene),
Secondary minerals: serp: serpentine, tr: tremolite, chl: chlorite, Tlc: talc, Carb: carbonates, mt: magnetite, pn: pentlandite, mi: millerite, cpy: chalcopyrite, vt: violarite, aw: awaruite, cpn: chalcopentlandite, hm: hematite, gt: goethite
Veins: V: serpentine veins, Lv: lizardite veins, Cv: chrysotile veins
Melt-rock interaction evidences: plagio: plagioclase, ol cryst: olivine crystallization, cpx cryst: clinopyroxene crystallization

Table 2 : Bulk major and trace elements compositions of the smooth seafloor serpentinites.

		SMS 1-2-1	SMS 1-2-35	SMS 2-2-11	SMS 2-2-17	SMS 3-2-1	SMS 4-2-1	SMS 5-4-14	SMS 5-4-17	SMS 6-3-14	SMS 7-3-7	SMS 8-2-17	SMS 8-2-25	SMS 10-5-6	SMS 11-2-4	SMS 11-2-11	SMS 13-4-11	SMS 14-5-1	SMS 14-5-8	SMS 15-3-16	SMS 17-4-19	SMS 17-4-32	SMS 21-5-6	SMS 22-6-13	SMS 26-2-11	SMS 27-2-19	SMS 28-4-10	SMS 29-5-41	SMS 29-6-13	SMS 30-2-2	SMS 33-3-27	SMS 34-2-17
Major element concentrations (wt.%)																															
SiO_2		43.48	41.19	40.53	38.37	40.87	41.12	39.76	39.22	43.11	40.7	39.08	42.77	38.15	41.81	38.51	39.4	36.91	38.04	38.24	42.14	40.78	39.85	38.54	41.23	38.61	40.3	38.6	38.4	38.78	44.57	40.09
Al_2O_3		2.96	2.02	2.33	1.81	2.85	3.8	2.58	3.23	2.46	2.32	1.47	2.82	2.08	3.91	2.63	1.63	0.55	0.58	2.58	2.83	2.07	1.19	2.38	2.33	2.53	2.34	0.85	1.89	0.93	3.45	0.91
Fe_2O_{3T}		9.06	8.72	8.04	7.81	7.87	12.97	9.63	11.2	8.46	8.3	8.18	8.95	7.97	8.55	19.63	7.15	10.87	9.51	7.82	9.03	9.12	9.33	10.89	8.95	7.69	8.42	7.31	8.04	7.59	10.12	7.82
FeO		4.93	3.71	2.5	2.65	2.73	2.21	2.14	2.81	4.65	3.3	2.32	4.92	3.11	2.44	2.28	1.76	1.51	1.57	2.22	4.78	4.58	1.73	nd	2.76	2.51	2.39	2.27	2.74	1.66	3.02	1.53
MnO		0.12	0.12	0.12	0.09	0.12	0.15	0.12	0.2	0.13	0.12	0.1	0.13	0.11	0.14	0.16	0.09	0.16	0.07	0.1	0.14	0.13	0.12	1.17	0.14	0.13	0.12	0.1	0.12	0.09	0.16	0.09
MgO		36.12	35.52	35.18	36.3	32.76	27.59	32.46	30.68	36.74	35.73	37.4	35.13	33.24	31.57	25.82	37.11	35.55	35.93	36.08	34.24	37.9	34.2	30.45	33.27	35.46	35.89	35.95	36.65	37.39	28.94	37.08
CaO		2.98	1.93	0.76	< d.l.	2.63	3.75	1.96	2.46	3.17	1.63	< d.l.	3.41	6.11	3.53	1.69	< d.l.	< d.l.	< d.l.	< d.l.	2.68	1.99	1	2	2.24	1.19	1.1	1.99	0.22	< d.l.	3.67	0.31
Na_2O		0.19	0.19	0.14	0.16	0.17	0.58	0.35	0.25	0.19	0.1	0.08	0.15	0.17	0.26	0.81	0.12	0.2	0.24	0.23	0.13	0.09	0.29	0.38	0.2	0.11	0.1	0.12	0.12	0.16	0.3	0.08
K_2O		< d.l.	< d.l.	< d.l.	< d.l.	< d.l.	< d.l.	< d.l.	< d.l.	< d.l.	< d.l.	< d.l.	< d.l.	< d.l.	< d.l.	< d.l.	< d.l.	< d.l.	< d.l.	< d.l.	< d.l.	< d.l.	< d.l.	0.11	< d.l.	< d.l.	< d.l.	< d.l.	< d.l.	< d.l.	< d.l.	< d.l.
P_2O_5		< d.l.	< d.l.	< d.l.	< d.l.	< d.l.	< d.l.	< d.l.	< d.l.	< d.l.	< d.l.	< d.l.	< d.l.	< d.l.	< d.l.	< d.l.	< d.l.	< d.l.	< d.l.	< d.l.	< d.l.	< d.l.	< d.l.	< d.l.	< d.l.	< d.l.	< d.l.	< d.l.	< d.l.	< d.l.	< d.l.	< d.l.
L.O.I.		4.86	10.05	12.67	14.48	11.39	9.49	11.98	11.49	5.77	11.16	14.27	6.95	12.68	10.58	9.41	13.27	14.53	14.4	14.15	9.03	8.91	13.7	13.91	11.18	13.04	12.41	14.04	13.46	14.53	7.57	13.13
Total		99.76	99.74	99.76	99.02	98.67	99.56	98.83	98.73	100.03	100.05	100.58	100.32	100.51	100.35	98.67	98.77	98.76	98.78	99.19	100.31	100.99	99.67	99.96	99.54	98.76	100.68	98.94	98.91	99.46	98.89	99.51
Fe^{3+}/Fe_{tot}		0.39	0.53	0.65	0.62	0.61	0.81	0.75	0.72	0.39	0.56	0.68	0.39	0.57	0.68	0.87	0.73	0.85	0.82	0.68	0.41	0.44	0.79		0.66	0.64	0.68	0.65	0.62	0.76	0.67	0.78
Trace element concentrations																																
Li	ppm	3.2	3.5	7.3	5.2	6.9	8.3	8.8	2.7	2.6	3.2	3.5	2.7	2.7	8	6.2	6.7	2.1	3.1	6.6	1.2	0.9	4	10.8	6.3	3.8	5.7	2.1	3.6	3.5	9.2	4.5
B	ppm	40	60	76	80	69	82	68	50	49	38	69	33	73	58	115	50	91	69	67	25	25	83	64	67	63	71	44	50	54	48	60
Be	ppb	< d.l.	0.8	< d.l.	9.2	< d.l.	70.5	4	220.4	2.2	4.3	0.6	1.1	< d.l.	5.4	305.2	20	0.2	10	258.6	5.9	4.9	59	966.8	8.2	< d.l.	0.1	9.8	5.8	8.3	255.4	8.8
Sc	ppm	3	14	12	10	14	21	13	17	14	14	8	16	11	17	21	6	6	5	13	15	12	5	13	15	11	12	7	12	6	20	7
Ti	ppm	393	436	147	276	337	492	347	410	441	332	111	530	332	546	271	137	53	57	343	478	411	73	792	275	329	347	39	323	148	664	2
V	ppm	80	77	70	66	88	214	114	207	81	77	39	81	56	124	356	39	68	76	73	84	66	62	126	111	63	68	46	69	38	159	43
Cr	ppm	2202	1872	2541	2646	2536	3906	2675	3309	2662	2475	2193	1903	2243	3437	3431	2180	2218	2690	2775	2515	2338	1567	1893	3170	2157	2151	2360	3093	2357	3110	2285
Mn	ppm	804	861	857	674	817	1070	821	1410	916	818	746	901	820	935	1087	632	1069	518	709	1000	922	515	8463	994	883	829	675	866	641	1168	590
Co	ppm	99	108	101	98	91	130	122	144	108	98	106	101	101	93	120	95	129	89	87	107	107	69	204	119	87	96	98	99	97	122	98
Ni	ppm	1972	2051	1950	1828	1591	1708	2037	1764	2109	1885	2110	1850	1983	1605	1518	1985	1934	1913	1959	1971	2037	1248	1719	2027	1677	1859	1927	2216	2159	1532	1945
Cu	ppm	26	9	20	11	15	67	15	94	31	18	2	21	18	34	239	9	62	93	84	14	23	38	289	5	25	21	5	9	3	61	3
Zn	ppm	43	39	42	58	41	157	83	114	81	46	87	83	88	86	250	52	60	86	135	52	42	80	211	53	79	35	48	46	51	145	45
Ga	ppm	2	2	1.9	1.8	2.1	4	2.5	3.6	2	2.2	1.2	2.2	1.8	3.1	4.5	1.8	1	1.2	2.7	2.7	1.9	1.2	4	2	2	1.9	0.7	1.7	1.1	3.6	0.6
Ge	ppm	2.4	1.4	1.4	1.5	1.8	2	1.6	1.8	1.2	1.6	1.4	1.9	1.1	1.2	3.8	2	3.3	1.5	1.5	1.4	1.4	1.2	1.9	1.4	2.9	1.5	1.4	1.2	1.2	2	1.7
As	ppm	0.8	0.6	0.6	2.3	1.6	9.8	5.4	9.8	1.1	0.5	0.4	0.9	0.6	2.6	28	1	4.8	5.9	1.8	0.3	0.2	2.8	6.8	3.5	0.4	0.1	1.7	7.3	9.5	7.1	2.1
Se	ppb	12.9	13.4	13.8	14.9	12.9	14.2	14.8	15.3	15.4	12.3	14.8	14.3	14.8	14	14.3	13.5	15.3	14.7	14.1	14.6	13	< d.l.	16.3	14	14.3	13.2	13.4	15.8	16.6	11.5	13.9
Rb	ppm	0.2	0.2	0.2	0.2	0.2	0.4	0.2	0.1	0.1	0.1	0.1	0.1	0.1	0.2	0.4	0.2	0.1	0.2	0.2	0.1	0	0.2	1.6	0.3	0.1	0.1	0.1	0.1	0.1	0.5	0.1
Sr	ppm	23.6	49.9	3.6	3.7	8.2	14.5	8.1	10.3	12.3	4	3.2	130.2	849.2	5.4	21.7	3.9	7.1	11.3	4.1	1.9	32.2	5.7	71.4	9.7	104.9	3.0	345.8	11.9	3.2	9.0	3.3
Y	ppm	2.26	2.10	1.10	1.30	1.91	5.44	2.35	3.36	2.74	1.99	0.65	2.71	1.68	3.10	7.49	0.57	0.90	1.15	1.12	3.81	1.60	0.64	8.30	2.20	1.70	1.95	0.30	1.15	0.52	5.47	0.34
Zr	ppm	0.9	0.96	0.05	1.45	0.59	4.39	0.54	5.73	1.4	0.95	0.3	1.43	0.87	1.57	10.33	1.03	0.14	1.33	10.04	1.98	1.54	2.10	65.08	0.48	0.86	0.67	1.31	1.12	0.74	13.55	0.2
Nb	ppb	3.71	1.15	3.48	5.2	2.23	7.48	2.73	29.63	6.13	< d.l.	2.68	8.1	4.18	3.23	23.58	5.35	< d.l.	12.08	48.39	4.33	6.50	17.67	6365.03	5.7	6.88	< d.l.	14.76	25.52	3.84	750.71	18.12
Ru	ppb	8.05	2.82	11.02	16.94	< d.l.	4.47	3.45	1.38	3.7	< d.l.	3.23	< d.l.	3.75	5.06	6.34	< d.l.	10.56	< d.l.	2.48	2.36	2.3	10.86	2.18	3.86	< d.l.	< d.l.	15.25	13.03	11.51	4.04	< d.l.
Rh	ppm	< d.l.	< d.l.	< d.l.	< d.l.	< d.l.	< d.l.	< d.l.	< d.l.	< d.l.	< d.l.	< d.l.	< d.l.	< d.l.	< d.l.	< d.l.	< d.l.	< d.l.	< d.l.	< d.l.	< d.l.	< d.l.	< d.l.	< d.l.	< d.l.	< d.l.	< d.l.	< d.l.	< d.l.	< d.l.	< d.l.	< d.l.
Pd	ppb	< d.l.	< d.l.	< d.l.	< d.l.	< d.l.	< d.l.	< d.l.	< d.l.	< d.l.	< d.l.	< d.l.	< d.l.	11.96	< d.l.	< d.l.	< d.l.	< d.l.	< d.l.	< d.l.	< d.l.	< d.l.	< d.l.	< d.l.	< d.l.	< d.l.	< d.l.	< d.l.	< d.l.	< d.l.	< d.l.	< d.l.
Ag	ppb	9.82	8.59	5.82	12.87	5.86	12.01	9.66	19.6	11.02	5.32	3.53	12.73	10.27	4.57	14.75	5.57	6.44	13.52	64.67	10.48	17.21	3.01	76.77	4.76	8.87	9.46	9.41	18.72	30.18	15.92	10.11
Cd	ppb	48.47	53.73	47.22	58.86	72.34	118.86	80.71	79.83	65.08	41.78	29.57	39.09	41.04	62.84	173.81	61.15	79.22	73.36	41.64	18.05	18.14	41.4	175.4	74.08	45.91	25.33	30.55	57.09	54.82	106.84	54.68
In	ppb	7.9	10.67	9.54	5.6	7	17.72	12.08	14.2	25.89	7.29	29.96	13.63	28.02	12.93	< d.l.	2.47	< d.l.	8.65	9.62	14.29	11.6	< d.l.	39.28	9.01	13.96	8.62	< d.l.	8.57	4.84	17.78	2.12
Sn	ppm	0.01	< d.l.	< d.l.	< d.l.	< d.l.	0.23	0.07	0.1	0.86	< d.l.	0.03	0.04	0.17	< d.l.	0.07	< d.l.	0.01	< d.l.	0.72	0.19	0.02	< d.l.	0.64	0.02	1.77	0.02	0.02	0.14	0.15	1.46	< d.l.
Sb	ppm	0.22	0.13	0.09	0.19	0.36	3.5	1.2	3.91	0.14	0.11	0.07	0.07	0.1	0.62	9.5	0.18	0.8	1.19	0.22	< d.l.	< d.l.	0.68	3.45	1.2	0.08	0.04	0.22	0.15	0.39	1.96	0.29
Te	ppm	< d.l.	< d.l.	0.02	0.01	< d.l.	< d.l.	0.01	< d.l.	< d.l.	< d.l.	0.01	< d.l.	< d.l.	0.02	0.02	< d.l.	0.01	0.01	0.01	0.01	< d.l.	0.01	0.11	0.01	< d.l.	0.01	< d.l.	0.02	0.03	0.01	0.01
Cs	ppm	< d.l.	< d.l.	0.01	< d.l.	< d.l.	0.03	< d.l.	< d.l.	< d.l.	< d.l.	< d.l.	< d.l.	< d.l.	< d.l.	< d.l.	< d.l.	< d.l.	0.01	< d.l.	< d.l.	< d.l.	< d.l.	0.11	0.02	< d.l.	< d.l.	< d.l.	< d.l.	< d.l.	0.04	< d.l.
Ba	ppm	0.51	0.66	1.50	0.37	1.13	2.54	1.53	3.15	1.41	0.62	1.17	0.81	2.06	1.40	2.78	1.27	1.72	2.67	0.40	0.14	0.18	1.27	114.16	2.52	0.81	1.75	1.05	0.73	0.92	2.53	0.95
La	ppm	0.02	0.01	0.01	0.04	0.03	0.96	0.26	0.64	0.01	0.02	0.01	0.02	0.01	0.11	2.37	0.08	0.25	0.44	0.05	0.02	0.03	0.17	12.14	0.19	0.01	< d.l.	0.12	0.01	0.07	0.86	0.09
Ce	ppm	0.03	0.05	0.01	0.05	0.01	0.12	0.03	0.2	0.06	0.05	0.04	0.05	0.04	0.03	0.06	0.08	0.03	0.11	0.11	0.25	0.11	0.03	68.79	0.07	0.04	0.03	0.36	0.05	0.05	0.83	0.09
Pr	ppm	0.02	0.01	< d.l.	0.02	0.01	0.21	0.05	0.12	0.03	0.02	0.01	0.03	0.02	0.03	0.50	0.03	0.03	0.08	0.02	0.04	0.03	0.03	2.77	0.06	0.01	0.01	0.03	0.01	0.01	0.25	0.02
Nd	ppm	0.19	0.14	0.01	0.13	0.09	1.00	0.26	0.56	0.26	0.14	0.05	0.23	0.15	0.26	2.09	0.14	0.16	0.37	0.12	0.38	0.19	0.16	10.97	0.34	0.13	0.13	0.11	0.09	0.07	1.18	0.07
Sm	ppm	0.12	0.11	0.02	0.07	0.08	0.32	0.12	0.20	0.17	0.10	0.03	0.16	0.09	0.18	0.52	0.05	0.03	0.08	0.07	0.27	0.10	0.04	2.50	0.13	0.09	0.10	0.03	0.07	0.03	0.39	0.02
Eu	ppm	0.06	0.04	0.01	0.03	0.03	0.12	0.05	0.06	0.07	0.04	0.01	0.07	0.04	0.07	0.15	0.02	0.01	0.02	0.03	0.10	0.04	0.01	0.60	0.09	0.04	0.05	0.02	0.03	0.02	0.10	0.01
Gd	ppm	0.24	0.21	0.07	0.14	0.17	0.57	0.22	0.36	0.31	0.20	0.05	0.28	0.18	0.34	0.75	0.07	0.05	0.10	0.13	0.46	0.17	0.06	2.47	0.21	0.18	0.21	0.04	0.14	0.07	0.58	0.02
Dy	ppm	0.36	0.32	0.15	0.20	0.28	0.77	0.32	0.53	0.43	0.31	0.09	0.41	0.27	0.49	0.98	0.09	0.06	0.13	0.19	0.63	0.26	0.09	2.29	0.31	0.26	0.31	0.04	0.20	0.09	0.80	0.02
Ho	ppm	0.08	0.08	0.04	0.05	0.07	0.18	0.08	0.12	0.10	0.07	0.02	0.10	0.06	0.11	0.24	0.02	0.02	0.03	0.04	0.14	0.06	0.02	0.44	0.08	0.06	0.07	0.01	0.05	0.02	0.18	0.01
Er	ppm	0.25	0.24	0.13	0.15	0.22	0.57	0.25	0.38	0.29	0.23	0.08	0.30	0.19	0.35	0.79	0.06	0.06	0.11	0.13	0.41	0.19	0.07	1.24	0.23	0.19	0.22	0.03	0.14	0.05	0.56	0.03
Tm	ppm	0.04	0.04	0.02	0.02	0.04	0.10	0.04	0.06	0.05	0.04	0.01	0.05	0.03	0.05	0.14	0.01	0.01	0.02	0.02	0.06	0.03	0.01	0.18	0.04	0.03	0.04	0.01	0.02	0.01	0.09	0.01
Yb	ppm	0.27	0.27	0.16	0.17	0.25	0.69	0.28	0.42	0.3	0.25	0.1	0.32	0.19	0.36	1.08	0.08	0.08	0.15	0.15	0.42	0.22	0.08	1.21	0.25	0.22	0.24	0.04	0.15	0.04	0.63	0.04
Lu	ppm	0.04	0.04	0.03	0.03	0.04	0.11	0.04	0.06	0.05	0.04	0.02	0.05	0.03	0.06	0.18	0.01	0.02	0.03	0.02	0.06	0.04	0.01	0.18	0.04	0.04	0.04	0.01	0.02	0.01	0.10	0.01
Hf	ppm	0.06	0.06	< d.l.	0.04	0.04	0.07	0.04	0.07	0.08	0.06	0.01	0.09	0.05	0.1	0.04	0.03	0.01	0.01	0.07	0.15	0.06	0.01	1.18	0.03	0.05	0.05	0.02	0.05	0.03	0.25	< d.l.
Ta	ppb	< d.l.	< d.l.	< d.l.	< d.l.	2.64	< d.l.	< d.l.	< d.l.	< d.l.	< d.l.	< d.l.	< d.l.	< d.l.	< d.l.	< d.l.	< d.l.	< d.l.	< d.l.	< d.l.	< d.l.	< d.l.	< d.l.	79.98	< d.l.	< d.l.	< d.l.	2.5	1.78	< d.l.	41.1	< d.l.
Re	ppb	< d.l.	< d.l.	< d.l.	< d.l.	< d.l.	< d.l.	< d.l.	< d.l.	< d.l.	< d.l.	< d.l.	< d.l.	< d.l.	< d.l.	< d.l.	< d.l.	< d.l.	< d.l.	< d.l.	< d.l.	< d.l.	< d.l.	< d.l.	< d.l.	< d.l.	< d.l.	< d.l.	< d.l.	1.01	< d.l.	< d.l.
Ir	ppb	< d.l.	< d.l.	< d.l.	< d.l.	< d.l.	< d.l.	< d.l.	< d.l.	< d.l.	< d.l.	< d.l.	< d.l.	< d.l.	< d.l.	1.25	< d.l.	< d.l.	< d.l.	< d.l.	< d.l.	< d.l.	< d.l.	1.14	< d.l.	< d.l.	< d.l.	< d.l.	< d.l.	< d.l.	< d.l.	< d.l.
Pt	ppb	3.32	3.45	2.17	2.68	4.82	2.69	4.91	6.74	6.84	4.92	2.84	4.50	3.60	4.88	52.13	1.30	5.09	< d.l.	3.90	5.30	5.40	2.00	14.22	3.17	3.30	3.32	6.34	4.98	1.88	7.37	4.30
Au	ppb	< d.l.	< d.l.	< d.l.	1.62	< d.l.	< d.l.	< d.l.	< d.l.	2.44	< d.l.	1.08	1.85	1.98	< d.l.	2.09	< d.l.	< d.l.	< d.l.	< d.l.	2.85	1.81	< d.l.	3.71	< d.l.	< d.l.	< d.l.	< d.l.	< d.l.	< d.l.	3.31	< d.l.
Tl	ppm	0.02	0.02	0.21	0.08	0.16	0.24	4.16	0.17	0.09	0.17	0.07	0.02	0.01	0.35	0.17	0.71	0.68	0.31	0.39	< d.l.	< d.l.	0.22	10.15	0.05	0.04	0.08	0.27	0.27	0.52	3.75	0.65
Pb	ppm	< d.l.	0.06	< d.l.	0.01	0.05	0.01	< d.l.	0.3	0.03	0.02	0.05	0.01	0.49	0.04	0.09	0.01	0.03	0.05	5.33	0.03	0.43	0.04	48.26	0.02	0.02	< d.l.	0.18	< d.l.	< d.l.	0.02	0.01
Bi	ppb	< d.l.	< d.l.	< d.l.	1.5	< d.l.	< d.l.	< d.l.	2.35	1.98	< d.l.	2.43	1.90	2.28	1.17	< d.l.	< d.l.	2.29	2.16	92.98	2.65	1.75	< d.l.	965.29	12.87	3.20	< d.l.	1.04	4.64	< d.l.	6.73	< d.l.
U	ppm	0.36	0.47	0.15	0.72	0.48	0.60	0.41	0.50	0.38	0.47	0.44	0.34	0.83	0.41	1.20	0.32	0.79	0.72	0.46	0.03	0.12	0.48	0.66	0.56	0.74	0.07	0.53	0.93	0.85	0.35	0.64

Abbreviations: < d.l.: below detection limit, L.O.I. : Loss on Ignition